Ultrasonic Waves in Solids Radiated from an Elliptically Loaded Source

by

Quanlin Zhou

M.S., Mechanics, Peking University (1996)

B.S., Mechanics, Tianjin University (1993)

Submitted to

the Department of Civil & Environmental Engineering

in Partial Fulfillment for the Degree of Master of Science

at the

Massachusetts Institute of Technology

July 2000

Signature of Author .....

Department of Civil & Environmental Engineering

July 2000

Certified by .....

Shi-Chang Wooh

Associate Professor of Civil & Environmental Engineering

Thesis Supervisor

Accepted by .....

Daniele Veneziano

Chairman, Department Committee on Graduate Students

Ultrasonic Waves in Solids Radiated from an Elliptically Loaded Source

by

Quanlin Zhou

Submitted to
the Department of Civil & Environmental Engineering
on July 31, 2000 in partial fulfillment of the
requirements for the Degree of Master of Science

Abstract

This thesis focuses on the directivity analysis of laser-generated ultrasound originated from a surface modified by water or other liquids. An improved mathematical model is developed to take into account the wet surface condition, which is described by an elliptical distribution of loads in the radiation source. Both circular and line sources are considered. The solutions for these sources are obtained by using Fourier and Bessel-Fourier transforms, respectively, and the transform integrals are evaluated asymptotically. The differences between the new model and the conventional constant loading model are discussed by comparing the directivities. The theoretical models are experimentally verified using a Nd:YAG pulsed laser as a source illuminated on wet and dry surfaces, the directivities are experimentally obtained by a laser interferometer and piezopolymer transducer. Experiments are carried out for various frequencies and source beam size. The experimental results are in good agreement with the theoretical predictions. The influence of source beam size, frequency and the elliptical parameter are discussed.

Thesis Supervisor: Shi-Chang Wooh

Title: Associate Professor of Civil & Environmental Engineering

ACKNOWLEDGEMENTS

First I would like to thank my thesis advisor Professor Shi-Chang Wooh for his continuous support. His enthusiasm, committment and his invaluable advices have made most important contributions to my research. He has also provided the generous funding that has sustained my two-year study at MIT.

I am grateful to my colleague Jiyong Wang who had been working on this project together with me. Also contributed to this project is Yijun Shi. Their help is deeply appreciated. I also thank Karen Veroy, Jung-Wuk Hong and Mark Orwat for their great support.

I would also like to thank Professor Louis Bucciarelli, without whom I might not have the opportunity of studying at MIT.

My family have supported me greatly through their continued confidence in me and their friendly correspondence.

This project was funded by Federal Railroad Administration, and formerly by American Association of Railroad.

Contents

List of Figures

List of Tables

Chapter 1

Introduction

1.1 Nondestructive evaluation and its methods

Nondestructive evaluation (NDE) is a common tool used in modern industry and scientific research for detecting flaws in materials. It has been almost exclusively used to detect macroscopic discontinuities in structures after they have been in service for some time [1]. Several advantages have made NDE a very popular approach for flaw detection. The most attractive advantage of NDE is that it can help keep the integrity of the structures or components, so that the properties and performance of the objects under examination are not damaged. The diversity of NDE methods is another advantage of NDE. An inspector can choose from various NDE methods according to its cost, safety, reliability and other features. Nowadays, NDE is widely employed in many application areas such as material characterization, visual inspection, welding, flaw detection and so forth.

Many different standard NDE approaches [2] exist, for example, as listed below:

1. *Radiographic Testing* uses a form of penetrating radiation, such as X-rays, Gamma or neutron rays, to evaluate the physical integrity of structures and materials. It can be used to detect internal flaws on a wide range of geometries and materials. Its

disadvantages include high cost and that its incapability of detecting tight laminar flaws or very tight cracks.

2. *Computed Tomography* is a method that uses computer to reconstruct the two-dimensional image of the cross section of an object. It can be achieved by using several different types of energy such as ultrasound, electrons, etc.. Its advantages and disadvantages are similar to those of Radiographic Testing, but it is applicable to three dimensional cases.

3. *Magnetic Particle Testing* detects surface or near surface discontinuities by finding the distortion of the magnetic fields associated with such discontinuities. The procedure is easy to implement. Also the required instrument is portable. But it is limited to ferromagnetic materials and near surface flaw detection only.

4. *Infrared Imaging* identifies material defects by detecting minute temperature differences of objects. This technique can realize non-contact and real-time detections. But the detection may be sensitive to the ambient temperature situations and the surface conditions of objects.

5. *Liquid Penetrant Testing* detects surface discontinuities in metallic and selected non-metallic materials by applying the penetrant to the surface. This procedure is of low cost and easy to implement. But it is limited to the surface flaws and the flaw depth is hard to estimate.

6. *Eddy Current Testing* takes advantage of the eddy currents, induced by placing an energized conducting coil near the surface of metallic material. The discontinuities of objects can be found by detecting the distortions of the magnitude and phase of the induced current. This procedure is easy to be automated and the required instrument is portable. But it is very sensitive to the geometric conditions and the results are difficult to be interpreted.

7. *Ultrasonic Testing* employs ultrasonic waves to detect surface or internal defects. Ultrasonic waves are the elastic waves generated above the audible range (typically 20 kHz). Compare with other NDE methods, the significant advantage of ultrasonic techniques is relative inexpensiveness. This method is best at crack detection and sizing, and its procedure may be automated. The limitation of ultrasonic testing is that it generally requires couplants in detection.

This paper presents some results on ultrasonic testing techniques which are among the prominent approaches for NDE.

1.2 Ultrasonic Testing

Ultrasonic techniques have made great development in the past 50 years because of the good properties of ultrasound in various mediums [1, 3–5]. First, due to the high frequency and short wavelength of ultrasound (the frequency range normally employed in ultrasonic nondestructive testing is from 100 kHz to 50 MHz), ultrasound can be reflected from very small surfaces such as internal defects. Consequently, it can detect internal and surface defects, evaluate microstructures, mechanical properties, as well as microscopic and macroscopic discontinuities in solid materials and structures. Second, ultrasonic testing can be used in testing relatively thick metallic samples, such as aluminum, because an ultrasonic beam travels with little loss through homogeneous materials. Third, a very promising feature of ultrasonic testing is its fast response which permits rapid and automated testing. Fourth, compared with other NDE methods, ultrasonic testing has better performance in locating defects and estimating the size of defects. However, the limitation of ultrasonic testing has to be mentioned here. Good geometry of tested objects is preferred in ultrasonic testing because it may be difficult to test an object with irregular shapes. Furthermore, the detection results are somewhat affected by the features of internal defects. Irregular boundary of the internal defects may give a result which is hard to be interpreted.

Typically, ultrasonic testing is conducted in through-transmission and pulse-echo mode with pulsed or continuous waves. In through-transmission mode, ultrasonic energy is transmitted through the test objects. This mode can be used in the characterization of materials such as the thickness measurement, and to detect internal defects if the size of the defect is larger than the wavelength of transmitted ultrasound. The principle of pulse-echo mode is to send ultrasound into objects and receive the echos reflected from discontinuities. This technique is one of the most widely used and versatile of ultrasonic testing for NDE, which can be used to locate discontinuities and measure the depths.

There are several means to generate and receive ultrasound:

1. *Piezoelectric transducer* (PZT) is the most popular way to generate and receive ultrasound. The principle is that, when a piezoelectric transducer is subjected to a high frequency voltage, it generates a high frequency vibration which results in an ultrasound wave in the object. And conversely, when a PZT is subjected to stress, a corresponding voltage is generated between its two surfaces.

2. *polyvinylidene fluoride* (PVDF) is another ultrasonic source, which has the same feature as piezoelectric materials, but is more sensitive to mechanical stresses and operates over a broader frequency range.

   In general, these two kind of transducers require couplant to get better propagation between two media. Due to the limitation of couplant, non-contact ultrasonic transducers are investigated.

3. *Electromagnetic acoustic transducer* (EMAT) is a non-contact transducer. The principle of an EMAT transmitter is that, when a current is induced to flow in the surface of the sample by means of a coil close to the surface, a solenoid at the surface generates a magnetic field perpendicular to the flow of current, so that a force is exerted on the material carrying the current. This localized stress field acts as an ultrasonic

source. In the EMAT receiver, the magnetic field is arranged so that movement of the surface causes an EMF to be induced in sensing coil.

4. *Laser* can also be used to generate ultrasound. Its particular advantage is the non-contact ultrasonic testing. The principle of laser-generated ultrasound is that, when a laser beam is induced on the surface of a sample, the localized heating produced by the laser generates the thermoelastic stresses and strains that act as an ultrasonic source. Besides, laser can also be used ultrasonic detection. One of the laser ultrasound detection techniques is laser interferometry. The optical interferometry between a reference laser beam and the laser reflected from or scattered by a surface subject are used to detect ultrasonic displacements.

1.3 Directivity patterns of laser-generated ultrasound

Recently laser has captured increasing attention. Non-contact generation and detection is an apparent advantage of laser over the contact transducers. In addition, laser can be used over a sufficiently wide temperature range which is beyond the reaches of most ultrasound techniques. Also laser is a broad-band ultrasound source while many conventional transducers have a relatively narrow bandwidth. Furthermore, laser beams can be made extremely small to give good access in confined spaces, but conventional transducers are limited by their sizes in such applications. Due to the advantages of laser ultrasonics, it has been used in diverse fields such as spectroscopy, metrology, inspection, communications, fusion research, weapons systems and surgery and so forth.

One of the important aspects of laser-generated ultrasound is its directivity pattern. Directivity pattern of ultrasound describes the spatial distribution of power of an ultrasound beam as a function of propagation angles. Therefore, only with a profound understanding of directivity can one apply laser-generated ultrasound technique correctly and effectively, which is the focus of this study.

Considerable efforts have been invested in the research of directivity patterns of ultrasound. The earliest work was done by Miller and Pursey [6] in the 1950s, where they studied the displacement field at an arbitrary point in a semi-infinite isotropic solid due to prescribed periodic stresses on the free surface. Although laser ultrasound technique was not discussed in this paper, it has been later the foundation of many researches on directivity. In the 1980s, many researchers investigated the generation of acoustic waves in metals by pulsed laser irradiation for various laser power densities [7–14]. Among these work, Scruby *et al.* [7] first conducted a comprehensive study of the use of laser for generating ultrasound. Hutchins *et al.* [9] carried out several experiments of directivity measurements to verify the theoretical prediction from Ref. [6]. They concluded that, for irradiation of a free metal surface by laser beams of low power density, the acoustic source formed by thermal expansion is characterized principally by stresses parallel to the metal surface; while in the presence of material ablation at higher power densities, stresses normal to the metal surface become the dominant source characteristic due to momentum transfer from ablating particles. Also he indicated that for small or thin laser beams, the experimental results were in good consistency with the theoretical prediction, but the results deteriorate with increasing source diameters. Rose [12] later pointed out that the point source derived by Scruby *et al.* [7] was somewhat speculative in thermoelastic regime. He proposed a point-source model, Surface Center of Expansion (SCOE), for laser-generated ultrasound, which better represents the tangential surface traction on a target. Later, several researchers have made more progress in the directivity analysis in thermoelastic regime. Zhang *et al.* [16] considered the thermal diffusion in laser-generated ultrasound, and found that the thermal diffusion has certain influence on the longitudinal directivity pattern. Wu *et al.* [17] further studied the directivity of laser-generated ultrasound in solids by solving thermoelastic wave equations, and concluded that thermal diffusion, optical absorption, ultrasonic frequency, and the diameter of source all have effects on the directivity. Hopko and Ume [18] studied the development of longitudinal directivity patterns from ablation to thermoelastic regime. At the same time, a point-source representation for laser-generated ultrasound in an elastic,

transversely isotropic half-space was developed by Hurley *et al.* [19]. Recently, Bernstein *et al.* [20] proposed a simplified laser line source model in aluminum which assumes no thermal conduction, and concluded that the amplitude directivity of a laser line source is identical to that of a point source in the plane perpendicular to the line axis while the temporal dependence differs. Besides the study in metals, many researchers also investigated laser-generated ultrasound in non-metals materials for different ultrasonic sources [21–23].

A very important aspect of directivity analysis is the surface condition of objects. The ultrasonic source can be divided into three categories: thermoelastic, ablated and modified surface sources. Past researches were focused on the thermoelastic and ablated sources that create uniform distributed loads on a free surface as shown above, while few works [9–11,24], mainly experimentally, have been done for modified surface sources. But in many important circumstances, the surface is modified by water, oil or other liquids. Such modifications may be the results of uncontrollable conditions, or due to the deliberate effort to obtain better outcomes. One example for the latter case is the detection of defects in a specimen. By spraying water drops on the surface of the specimen, one can expect better results. As a result of surface modification, the stress distribution on the modified surface will be affected by the momentum transfer from the liquids, and then may not be necessarily uniform. My experiments, which will be introduced in Chapter 3, show that the directivity patterns on modified surfaces are different from those of free or uniformly ablated surfaces.

This paper proposes an elliptically distributed radiation source as the boundary condition on a surface, which represents the condition where the object surface is modified by water or other liquids. For the acoustic source, we are only interested in the power range where ablation occurs for dry surfaces. It had been observed, in past research, the directivity profiles of modified surfaces are qualitatively close to those of ablated surfaces. This conclusion is frequently used in predicting the directivities of modified surfaces. However, the theoretical results developed in this thesis indicate that apparent difference between the two cases, The Fourier or Fourier-Bessel Transform and the asymptotic method are applied

in the analytical derivation. Comparison is made between this source and ablation source for which existing theoretical results are available. It turns out that the directivity is determined by $J_2(x)/x^2$ (where $J_2(x)$ is the second order Bessel function) for the elliptical distribution source, while $J_1(x)/x$ ($J_1(x)$ is the first order Bessel function) determines the directivity in constant loading source. Several experiments are carried out to verify this model. Chapter 2 discusses the theoretical derivation of the elliptical distribution model, and the comparison between this model and the constant loading which corresponds the ablated source. Chapter 3 discusses the experimental setup and directivity measurements using laser-generated ultrasound. Chapter 4 includes the discussion and conclusions.

Chapter 2

Directivity Analysis

2.1 Definition of directivity pattern

In general, when an object is excited by an acoustic source on the surface of a solid, as shown in Fig. 2-1, the sound pressure at point B varies with radiation angle θ, given the

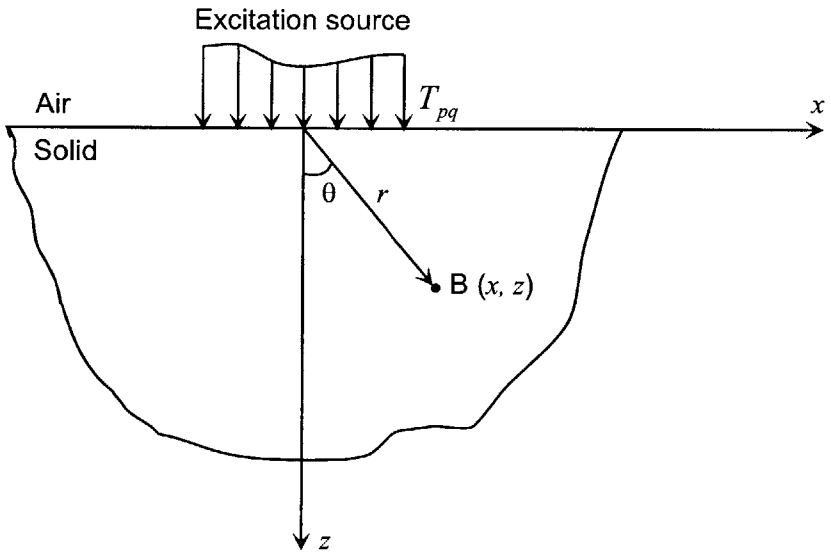

Figure 2-1: The coordinate plot when an acoustic source excites on a specimen.

fired distance r from the excitation origin. The sound pressure plotted as a function of radiation angle indicates the directional dependence of the ultrasound propagation. This dependence is referred to as the *directivity pattern* of the corresponding radiation source. Since our research focuses on the laser-generated ultrasound, the directivity analysis is focused on the field of laser ultrasonics.

2.2 Source loading

Acoustic sources generated by laser irradiation can be categorized into two main sources based on the illumination shape: *circular* and *line* sources, as shown in Fig. 2-2. Circular sources produce waves with spherical symmetry, and thus the directivity patterns are spherically symmetric. A point source is a special case of circular sources, where the radius of the source approaches zero. It is generally assumed that a circular source consists of an assembly of infinitely large number of point sources over its area. By focusing the incident laser beam with a cylindrical lens to form an illuminated line segment, we can get a line source that produces two-dimensional waves with cylindrical symmetry.

Furthermore, from the perspective of excitation mechanism of laser-generated ultrasound, acoustic sources can be classified into two types, as shown in Fig. 2-3, depending

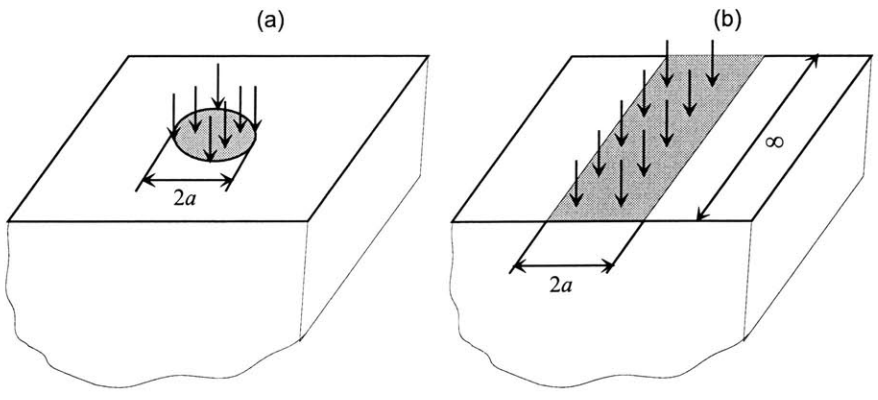

Figure 2-2: Laser loading geometries: (a) circular loading, (b) line loading.

on the source intensity: *ablation* sources driven by spatially uniform normal stresses, and *thermoelastic* sources produced by uniform surface shear stresses on the illuminated area of the free surface. Thermoelastic sources can be created by the irradiation of the surface with a pulsed laser, whose incident optical power densities is below that required for material ablation and subsequent plasma formation. In this case, a significant thermal diffusion takes place in the sample within the time duration of the laser pulse. Compared with the shear stresses caused by thermal expansion acting in the direction parallel to the sample surface, normal stresses are negligible. A thermoelastic source can thus be represented as a point dilation (center of expansion) at the surface.

As the incident power density increases, the surface temperature increases till the melting point of the sample is reached. By further increasing the power density, evaporation and ablation are resulted on the sample surface. A laser source with such power density is called the ablation source. In this case, the thermoelastic stresses are so small that they can be neglected, and ablation is represented as a time-varying force acting normal to the surface.

If the surface condition of an object is modified by water or other liquids, the momentum transfer from the evaporation of liquids under the laser irradiation becomes the acoustic source, whose directivity pattern was thought to be close to that of the ablation source [9–11]. However, the ablation source is caused by spatially uniform normal stresses due to the material ablation, while the stresses caused by the liquid evaporation is not nec-

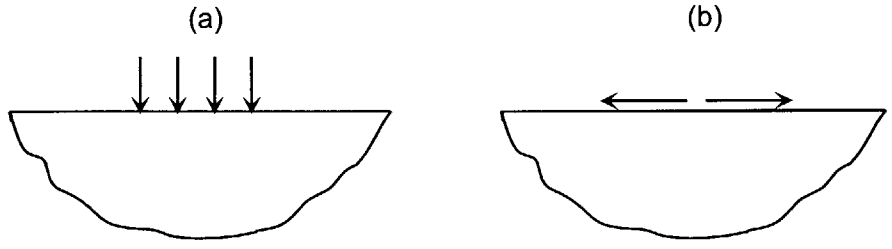

Figure 2-3: Laser excitation sources: (a) ablation source, (b) thermoelastic source.

essarily spatially uniform. This yields the difference of the directivity patterns between these two sources.

The following sections provides the theoretical derivation of the directivity patterns for the surface modified source by solving wave propagation equation. The results of ablation sources are included as a comparison.

2.3 Basic equations of propagation and boundary conditions

The equation of motion in elastic isotropic solids is expressed in vector form as

$$(\lambda + 2\mu)\nabla\nabla \cdot \mathbf{u} - \mu\nabla \times \nabla \times \mathbf{u} = \rho\frac{\partial^2 \mathbf{u}}{\partial t^2} , \tag{2.1}$$

where $\mathbf{u}$ is the displacement vector, ρ the mass density, λ and μ the Lamé constants of the medium, and ∇ is the gradient operator. This equation may be solved for the displacements but the boundary condition are prescribed in terms of stresses. For a circular laser source of radius a or a line source of width $2a$ illuminated on a half space, the surface traction can be generally expressed as a time harmonic function:

$$\bar{T}_{pq}(x,t) = \begin{cases} T_{pq}(x)e^{j\omega t}, & \text{for } |x| < a \\ 0, & \text{for } |x| > a \ , \end{cases} \tag{2.2}$$

where x is either the distance for a line source, or the radial distance R for a circular source, of a point on the surface from the center of the excitation source, ω the excitation frequency, j the unit imaginary number, p and q are the indices to denote the coordinates. By solving Eq. (2.1) with the boundary conditions (2.2), we may obtain the transient solutions, but we are only interested in the steady-state solutions in this paper, so that we are only considering the traction amplitude $T_{pq}(x)$.

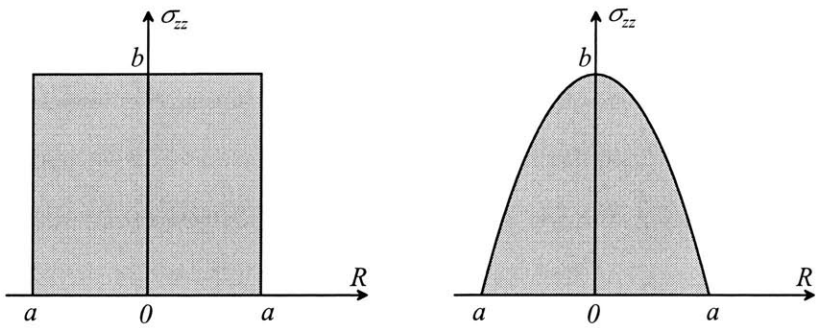

Figure 2-4: The loading distribution on the free surface: (I) the constant stresses; (II) the elliptical distribution.

We will consider two different loading conditions, ideally representing dry or wet surfaces (Case I and II). The normal traction T_{zz} for dry surfaces are typically modeled as a constant loading of magnitude b over the illuminated area, while the shear traction T_{zx} are assumed to be zero everywhere, i.e., the traction amplitudes are

$$T_{zz}(x) = b, \quad \text{and} \quad T_{zx}(x) = 0\ , \tag{2.3}$$

where $T_{zx}(x)$ can be either $T_{zR}(R)$ for a circular source, or $T_{zx}(x)$ for a line source.

In order to deal with wet surfaces, we may propose an alternative expression:

$$T_{zz}(x) = b\left(1 - \frac{x^2}{a^2}\right), \quad \text{and} \quad T_{zx}(x) = 0\ . \tag{2.4}$$

This condition represents an elliptical distribution of traction with an aspect ratio of b/a, as shown in Fig. 2-4. This assumption may be validated by the following reasons. When a laser beam hits a wet surface, it is likely that the water evaporates rapidly. The evaporated water particles at the center will possibly cause greater reaction force in the direction normal to the surface. On the other hand, the water molecules near the illumination boundary

are surrounded by other neighboring molecules, so that the reaction forces may be nonuniformly distributed within the source area. By considering the specific heat of water, heat transfer and friction forces between the water molecules, we may assume that the reaction forces at the boundary are significantly smaller than that of the center of the source. We chose an elliptical distribution because it is handy for mathematical manipulations as will be shown later.

2.4 Circular source excited by normal stresses (radius = a)

In this section, we will consider Case II for circular source first. The wave propagation equation, combined with the elliptical distribution boundary condition, is solved using the Fourier-Bessel transform and asymptotic method [6]. Case I will be shown later.

2.4.1 The elliptical distribution model

Since the elliptical loading for the circular source is axisymmetric, the problem can be best formulated in cylindrical coordinates (R, ϕ, z). This becomes a two dimensional problem since the displacement components u_ϕ and its derivatives with respect to ϕ vanish. Defining

$$\nabla \cdot \mathbf{u} = \frac{1}{R}\frac{\partial (R u_R)}{\partial R} + \frac{\partial u_z}{\partial z} = \triangle \,, \tag{2.5}$$

and

$$\nabla \times \mathbf{u} = \left(\frac{\partial u_R}{\partial z} - \frac{\partial u_z}{\partial R} \right) \mathbf{i}_\phi = W \mathbf{i}_\phi \,. \tag{2.6}$$

and substituting these equations into Eq. (2.1), we get the equations of motion in the R and z directions as

$$(\lambda + 2\mu)\frac{\partial \triangle}{\partial R} + \mu\frac{\partial W}{\partial z} + \rho\omega^2 u_R = 0 \,, \tag{2.7}$$

$$(\lambda + 2\mu)\frac{\partial \triangle}{\partial z} - \frac{\mu}{R}\frac{\partial (RW)}{\partial R} + \rho\omega^2 u_z = 0 \,, \tag{2.8}$$

where u_R and u_z are the time harmonic displacements in the R and z directions respectively, and $\mathbf{i}_\phi$ is the unit vector in the ϕ direction. Substituting Eqs. (2.5) and (2.6) into the derivatives of these equations yields

$$\frac{1}{R}\frac{\partial}{\partial R}\left(R\frac{\partial \triangle}{\partial R}\right) + \frac{\partial^2 \triangle}{\partial z^2} + k_L^2 \triangle = 0 \,, \tag{2.9}$$

$$\frac{\partial}{\partial R}\left\{\frac{1}{R}\frac{\partial (RW)}{\partial R}\right\} + \frac{\partial^2 W}{\partial z^2} + k_T^2 W = 0 \,, \tag{2.10}$$

where k_L and k_T are the wavenumbers of the longitudinal and shear waves, respectively:

$$k_L = \omega\sqrt{\frac{\rho}{\lambda + 2\mu}}, \quad \text{and} \quad k_T = \omega\sqrt{\frac{\rho}{\mu}} \,. \tag{2.11}$$

These are the governing equations of the problem.

The boundary conditions require the expressions for the stresses in terms of displacements which can be obtained from the Hook's Law

$$\sigma_{zz} = \lambda \triangle + 2\mu\frac{\partial u_z}{\partial z} \,, \tag{2.12}$$

$$\sigma_{\phi z} = \mu \left(\frac{1}{R} \frac{\partial u_z}{\partial \phi} + \frac{\partial u_\phi}{\partial z} \right) = 0 \,, \tag{2.13}$$

$$\sigma_{zr} = \mu \left(\frac{\partial u_z}{\partial R} + \frac{\partial u_R}{\partial z} \right) \,, \tag{2.14}$$

or in explicit forms the normal and shear stresses are

$$\frac{\rho\omega^2}{\mu^2}\sigma_{zz} = \frac{2}{R}\frac{\partial}{\partial R}\left(R\frac{\partial W}{\partial z}\right) - \frac{k_T^2(k_T^2 - 2k_L^2)}{k_L^4 R}\frac{\partial}{\partial R}\left(R\frac{\partial \triangle}{\partial R}\right) - \left(\frac{k_T}{k_L}\right)^4 \frac{\partial^2 \triangle}{\partial z^2} \,, \tag{2.15}$$

$$\frac{\rho\omega^2}{\mu^2}\sigma_{zR} = \frac{\partial}{\partial R}\left\{\frac{1}{R}\frac{\partial (RW)}{\partial R}\right\} - \frac{\partial^2 W}{\partial z^2} - 2\left(\frac{k_T}{k_L}\right)^2 \frac{\partial^2 \triangle}{\partial R \partial z} \,. \tag{2.16}$$

In order to eliminate R from these equations, we use the Fourier-Bessel transform method. The Fourier-Bessel transform of a function $f(R)$ is defined as

$$\hat{f}_m(\zeta) = \int_0^\infty f(R) R J_m(\zeta R) dR \,, \tag{2.17}$$

and its inverse transform pair is written as

$$f(R) = \int_0^\infty \hat{f}_m(\zeta) \zeta J_m(\zeta R) d\zeta \tag{2.18}$$

where J_m is the Bessel function of the m-th order and ζ is the variable of integration. For example, the zero-order transform of σ_{zz} can be written as

$$\hat{\sigma}_{zz0} = \int_0^\infty \sigma_{zz} R J_0(\zeta R) dR \,. \tag{2.19}$$

Substituting Eq. (2.4) into (2.19) and using the property of the Bessel function

$$\frac{d[x^{\pm m}J_m(x)]}{dx} = \pm x^{\pm m}J_{m\mp 1}(x) \ , \tag{2.20}$$

the transform of σ_{zz} can be obtained as

$$\hat{\sigma}_{zz0} = \frac{2bJ_2(\zeta a)}{\zeta^2} \ . \tag{2.21}$$

And the transform of σ_{zR} is

$$\hat{\sigma}_{zR1} = 0 \ . \tag{2.22}$$

Similarly, the transforms of Eqs. (2.7), (2.8), (2.9), (2.10), (2.15) and (2.16) yield

$$\hat{u}_{R1} = -\frac{\mu}{\rho\omega^2}\left(\frac{d\hat{W}_1}{dz} - \frac{k_T^2}{k_L^2}\zeta\hat{\triangle}_0\right) \ , \tag{2.23}$$

$$\hat{u}_{z0} = -\frac{\mu}{\rho\omega^2}\left(\frac{k_T^2}{k_L^2}\frac{d\hat{\triangle}_0}{dz} - \zeta\hat{W}_1\right) \ , \tag{2.24}$$

$$\frac{d^2\hat{\triangle}_0}{dz^2} - (\zeta^2 - k_L^2)\hat{\triangle}_0 = 0 \ , \tag{2.25}$$

$$\frac{d^2\hat{W}_1}{dz^2} - (\zeta^2 - k_T^2)\hat{W}_1 = 0 \ , \tag{2.26}$$

$$\frac{\rho\omega^2}{\mu^2}\hat{\sigma}_{zz0} = -\frac{k_T^4}{k_L^4}\frac{d^2\hat{\triangle}_0}{dz^2} + 2\zeta\frac{d\hat{W}_1}{dz} + \frac{k_T^2}{k_L^2}\left(\frac{k_T^2}{k_L^2} - 2\right)\zeta^2\hat{\triangle}_0 \ , \tag{2.27}$$

$$\frac{\rho\omega^2}{\mu^2}\hat{\sigma}_{zR1} = -\left(\frac{d^2\hat{W}_1}{dz^2} - 2\zeta\frac{k_T^2}{k_L^2}\frac{d\hat{\triangle}_0}{dz} + \zeta^2\hat{W}_1\right) . \tag{2.28}$$

Solving Eqs. (2.25) and (2.26), we get far-field solutions

$$\hat{\triangle}_0 = Ae^{-z\sqrt{(\zeta^2-k_L^2)}} \quad \text{and} \quad \hat{W}_1 = Be^{-z\sqrt{(\zeta^2-k_T^2)}} . \tag{2.29}$$

which have finite values for large z. The constant A and B are determined by substituting Eqs. (2.21) and (2.29) into Eqs. (2.27) and (2.28) yields

$$\hat{\triangle}_0 = \frac{2b\rho\omega^2 k_L^2(k_T^2 - 2\zeta^2)}{\mu^2 k_T^2\zeta^2 G(\zeta)} J_2(\zeta a)e^{-z\sqrt{\zeta^2-k_L^2}} \tag{2.30}$$

$$\hat{W}_1 = \frac{4b\rho\omega^2\sqrt{\zeta^2 - k_L^2}}{\mu^2\zeta G(\zeta)} J_2(\zeta a)e^{-z\sqrt{\zeta^2-k_T^2}} \tag{2.31}$$

where

$$G(\zeta) = (2\zeta^2 - k_T^2)^2 - 4\zeta^2\sqrt{(\zeta^2 - k_L^2)(\zeta^2 - k_T^2)} . \tag{2.32}$$

Plugging these solutions into Eqs. (2.24) and (2.23) results in the transforms of the displacement components

$$\hat{u}_{z0} = \frac{2b\sqrt{\zeta^2 - k_L^2}J_2(\zeta a)}{\mu\zeta^2 G(\zeta)}\left\{2\zeta^2 e^{-z\sqrt{\zeta^2-k_T^2}} + (k_T^2 - 2\zeta^2)e^{-z\sqrt{\zeta^2-k_L^2}}\right\} , \tag{2.33}$$

$$\hat{u}_{R1} = \frac{2bJ_2(\zeta a)}{\mu\zeta G(\zeta)}\left\{2\sqrt{(\zeta^2 - k_L^2)(\zeta^2 - k_T^2)}e^{-z\sqrt{\zeta^2-k_T^2}} + (k_T^2 - 2\zeta^2)e^{-z\sqrt{\zeta^2-k_L^2}}\right\} . \tag{2.34}$$

To obtain the displacement components, we apply the inverse Fourier-Bessel Transform defined by Eq. (2.18) to the above equations:

$$u_z = \frac{2b}{\mu}\int_0^\infty \frac{\sqrt{\zeta^2-k_L^2}J_2(\zeta a)}{\zeta G(\zeta)}\left\{2\zeta^2 e^{-z\sqrt{\zeta^2-k_T^2}} + (k_T^2-2\zeta^2)e^{-z\sqrt{\zeta^2-k_L^2}}\right\}J_0(\zeta r)d\zeta\ , \tag{2.35}$$

$$u_R = \frac{2b}{\mu}\int_0^\infty \frac{J_2(\zeta a)}{G(\zeta)}\left\{2\sqrt{(\zeta^2-k_L^2)(\zeta^2-k_T^2)}e^{-z\sqrt{\zeta^2-k_T^2}} + (k_T^2-2\zeta^2)e^{-z\sqrt{\zeta^2-k_L^2}}\right\}J_1(\zeta r)d\zeta\ . \tag{2.36}$$

By using the asymptotic method [6], the integrals

$$I_1 = \int_0^\infty e^{-z\sqrt{\zeta^2-m^2}}J_0(R\zeta)\zeta\chi(\zeta)d\zeta\ , \tag{2.37}$$

and

$$I_2 = \int_0^\infty e^{-z\sqrt{\zeta^2-m^2}}J_1(R\zeta)\zeta^2\chi(\zeta)d\zeta \tag{2.38}$$

can be evaluated asymptotically for large positive values of z and R as

$$I_1 = \frac{jm}{r}e^{-jmr\cos\theta}\chi(m\sin\theta) + O(r^{-2})\ , \tag{2.39}$$

and

$$I_2 = -\frac{m^2}{r}e^{-jmr\cos\theta}\sin\theta\chi(m\sin\theta) + O(r^{-2})\ , \tag{2.40}$$

where $m = 1$ or $\frac{k_2}{k_1}$, $\chi(\zeta)$ is an even function of ζ and analytic at the origin, and

$$z = r\cos\theta \quad \text{and} \quad R = r\sin\theta\ . \tag{2.41}$$

Then u_z and u_R can be asymptotically evaluated as

$$u_z = \frac{j2b\cos\theta}{\mu r}\left\{\frac{2k_T\sqrt{k_T^2\sin^2\theta - k_L^2}J_2(k_T a\sin\theta)}{G(k_T\sin\theta)}e^{-jk_T r} + \frac{i\cos\theta(k_T^2 - 2k_L^2\sin^2\theta)J_2(k_L a\sin\theta)}{G(k_L\sin\theta)\sin^2\theta}e^{-jk_L r}\right\}, \tag{2.42}$$

$$u_R = \frac{j2b\cos\theta}{\mu r}\left\{-\frac{2k_T\cos\theta\sqrt{k_T^2\sin^2\theta - k_L^2}J_2(k_T a\sin\theta)}{G(k_T\sin\theta)\sin\theta}e^{-jk_T r} + \frac{j(k_T^2 - 2k_L^2\sin^2\theta)J_2(k_L a\sin\theta)}{G(k_L\sin\theta)\sin\theta}e^{-jk_L r}\right\}. \tag{2.43}$$

To obtain the radial and tangential displacement components of the field we introduce the new variables, U_a^L and U_a^T, and use the relation

$$U_a^L = u_z\cos\theta + u_R\sin\theta\ , \tag{2.44}$$

$$U_a^T = u_R\cos\theta - u_z\sin\theta\ , \tag{2.45}$$

to get the field in polar coordinates:

$$U_a^L(r,\theta) = \left(\frac{2a^2b}{\mu}\right)\left(\frac{e^{-jk_L r}}{r}\right)\left(\frac{J_2(\xi_L)}{\xi_L^2}\right)U_0^L(\theta)\ , \tag{2.46}$$

$$U_a^T(r,\theta) = \left(\frac{2a^2b}{\mu}\right)\left(\frac{e^{-jk_T r}}{r}\right)\left(\frac{J_2(\xi_T)}{\xi_T^2}\right)U_0^T(\theta)\ . \tag{2.47}$$

where

$$\xi_L = k_L a\sin\theta \quad \text{and} \quad \xi_T = k_T a\sin\theta, \tag{2.48}$$

$J_2(\xi)$ is the second order Bessel function, $U_0^L(\theta)$ and $U_0^L(\theta)$ are the far-field amplitudes of the compression wave radiated from a point source [9]

$$U_0^L(\theta) = \frac{-k_L^2(k_T^2 - 2k_L^2 \sin^2\theta)\cos\theta}{G(k_L \sin\theta)} , \tag{2.49}$$

$$U_0^T(\theta) = \frac{-jk_T^3\sqrt{k_T^2 \sin^2\theta - k_L^2}\sin 2\theta}{G(k_T \sin\theta)} . \tag{2.50}$$

2.4.2 The constant loading model

The case of constant stresses was derived by Miller [6]. The displacement amplitudes of the longitudinal and shear waves are:

$$U_a^L(r,\theta) = \left(\frac{a^2 b}{\mu}\right)\left(\frac{e^{-jk_L r}}{r}\right)\left(\frac{J_1(\xi_L)}{\xi_L}\right) U_0^L(\theta) , \tag{2.51}$$

$$U_a^T(r,\theta) = \left(\frac{a^2 b}{\mu}\right)\left(\frac{e^{-jk_T r}}{r}\right)\left(\frac{J_1(\xi_T)}{\xi_T}\right) U_0^T(\theta) . \tag{2.52}$$

As described by Hutchins [9], the term $a^2 b/\mu$ is the effective source strength and $e^{-jk_L r}/r$ represents the propagation of spherical wavefronts (longitudinal) from a point source whose directivity is determined by $U_0^L(\theta)$. These values are then modified by the $J_1(\xi)/\xi$ term, which is simply the factor taking into account the finite dimension of the circular source by assuming that the area consists of an assembly of infinitely large number of point sources over its area.

2.4.3 Directivity patterns of the two cases

It is interesting to note that the displacements of the two models have similar patterns except that they are modified by different factors $\frac{J_1(\xi)}{\xi}$ and $\frac{J_2(\xi)}{\xi^2}$. By normalizing the

displacements U_a^L and U_a^T defined in Eqs. (2.51) and (2.52) for Case I, and Eqs. (2.46) and (2.47) for Case II, the far-field directivities can be respectively obtained as

$$H_{a1}^L(\theta) = \frac{J_1(\xi_L)}{\sin\theta} H_0^L(\theta) \ , \tag{2.53}$$

$$H_{a1}^T(\theta) = \frac{J_1(\xi_T)}{\sin\theta} H_0^T(\theta) \tag{2.54}$$

for Case I, and

$$H_{a2}^L(\theta) = \frac{J_2(\xi_L)}{\sin^2\theta} H_0^L(\theta) \ , \tag{2.55}$$

$$H_{a2}^T(\theta) = \frac{J_2(\xi_T)}{\sin^2\theta} H_0^T(\theta) \tag{2.56}$$

for Case II, where $H_0^L(\theta)$ and $H_0^T(\theta)$ are the far-field directivities of point sources

$$H_0^L(\theta) = \frac{(k_T^2 - 2k_L^2\sin^2\theta)\cos\theta}{G(k_L\sin\theta)} \ , \tag{2.57}$$

and

$$H_0^T(\theta) = \frac{(k_T^2\sin^2\theta - k_L^2)^{1/2}\sin 2\theta}{G(k_T\sin\theta)} \ . \tag{2.58}$$

Obviously, the directivities are the functions of a, θ and wavenumbers.

As a comparison, the two directivity patterns are plotted together for some fixed a and certain frequencies. See Fig. 2-5 and 2-6 for the directivities at various a and 1 MHz frequency, and Fig. 2-7 and 2-8 for 5 MHz. It is observed that the difference between the two models is small at small a and low frequencies, but at larger a and higher frequencies, their difference is getting significant.

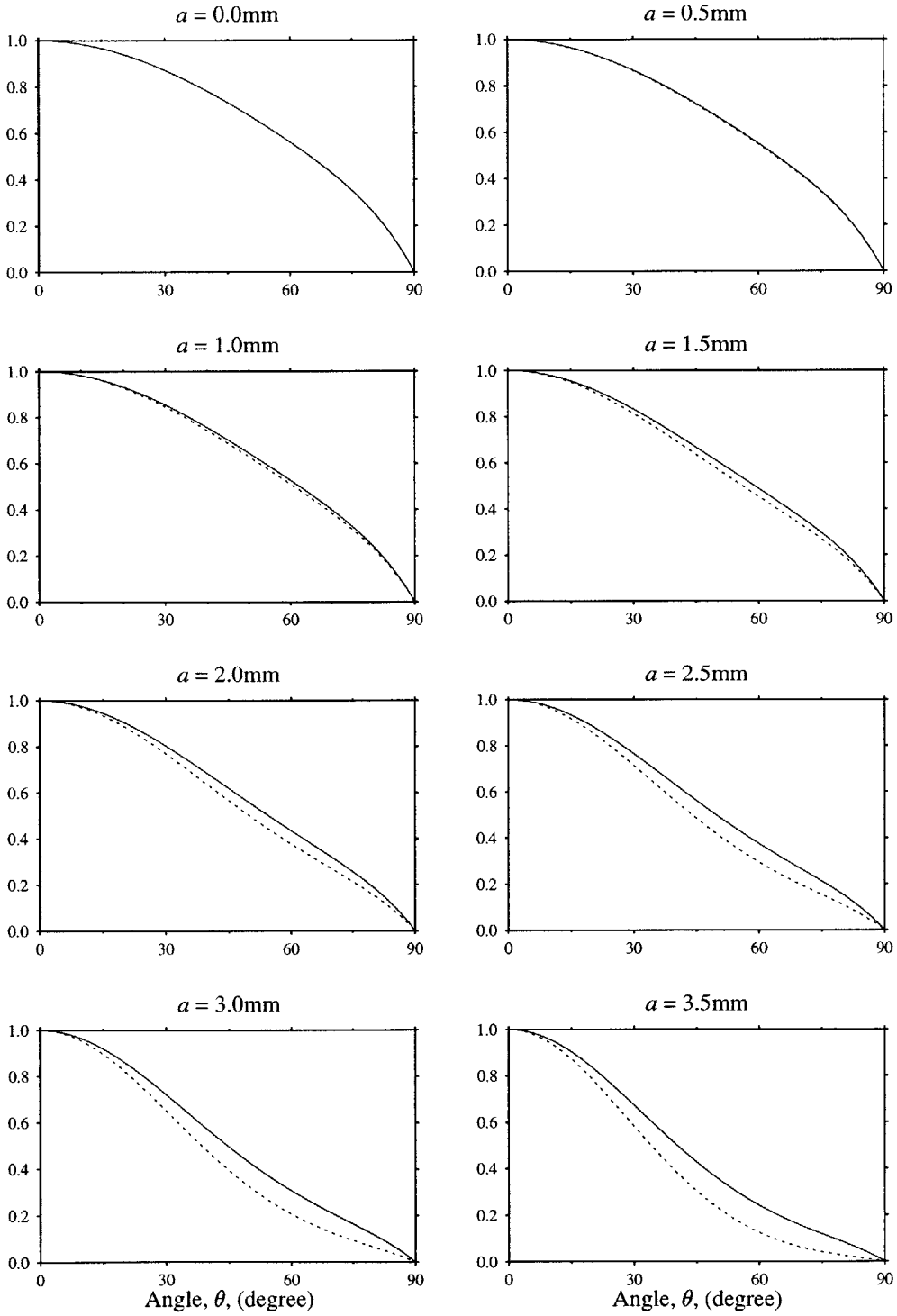

Figure 2-5: Directivities of longitudinal waves from the two models at 1 MHz and various a: solid line represents the elliptical distribution model and dash line the constant loading model.

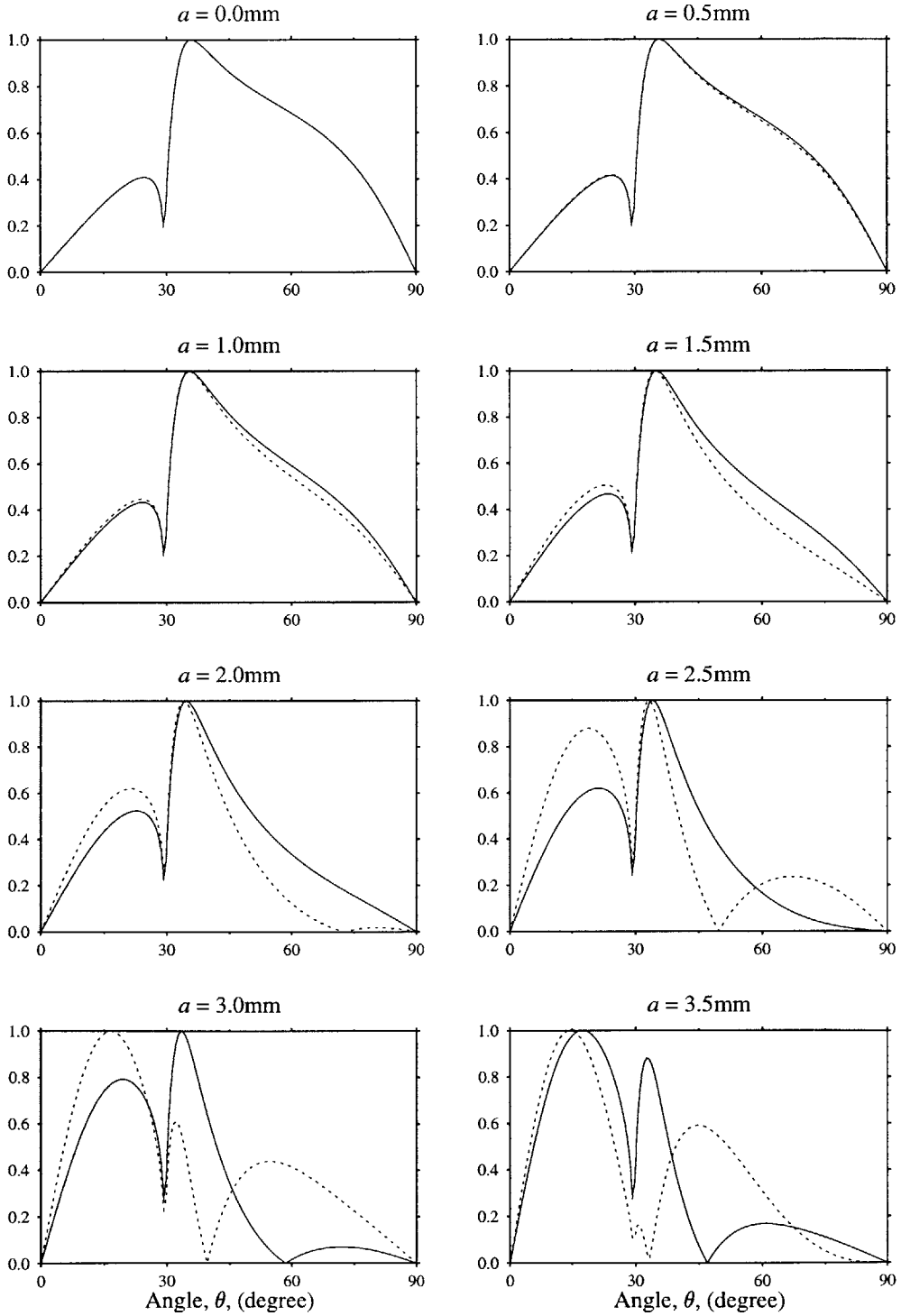

Figure 2-6: Directivities of shear waves from the two models at 1 MHz and various a: solid line represents the elliptical distribution model and dash line the constant loading model.

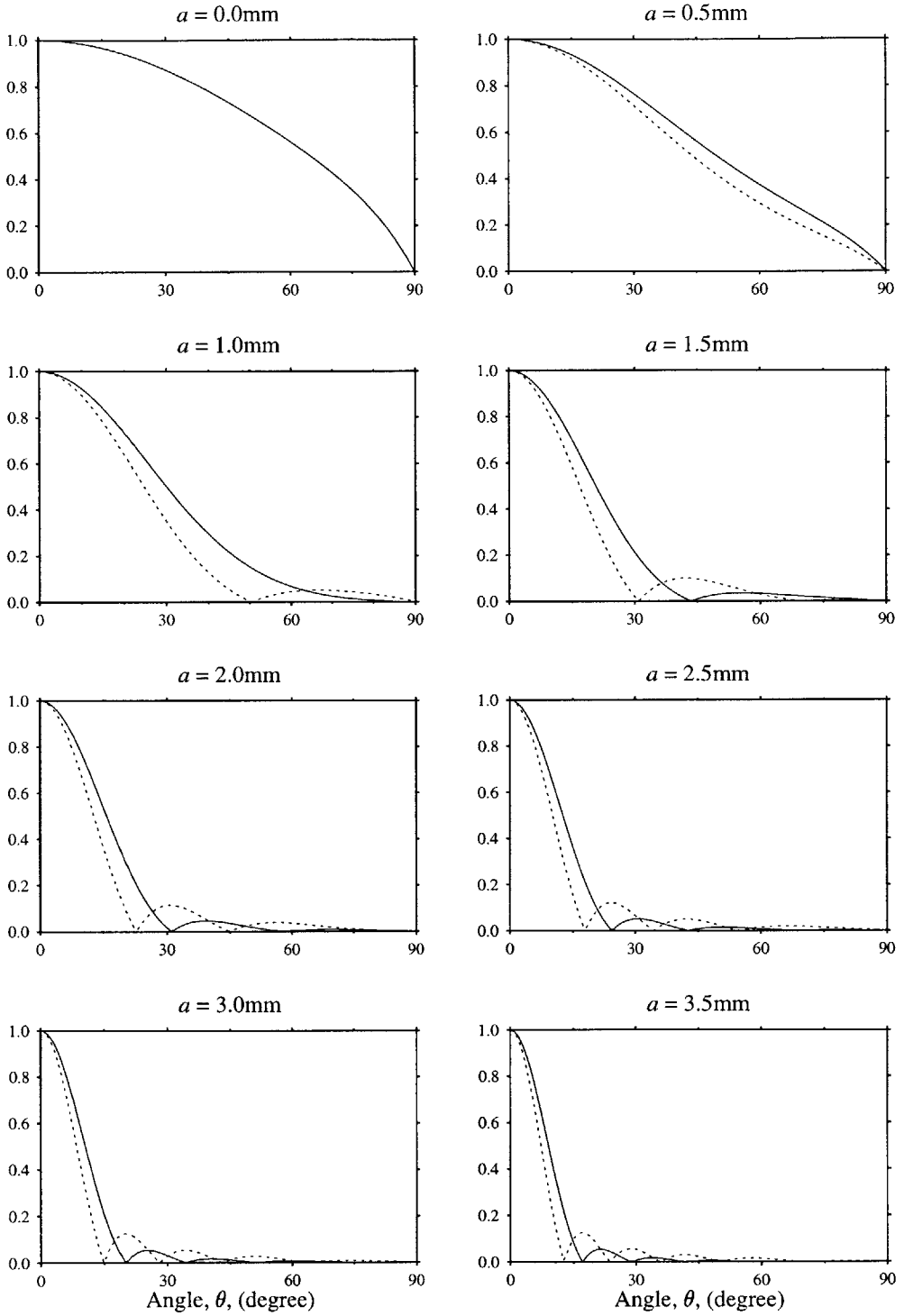

Figure 2-7: Directivities of longitudinal waves from the two models at 5 MHz and various a: solid line represents the elliptical distribution model and dash line the constant loading model.

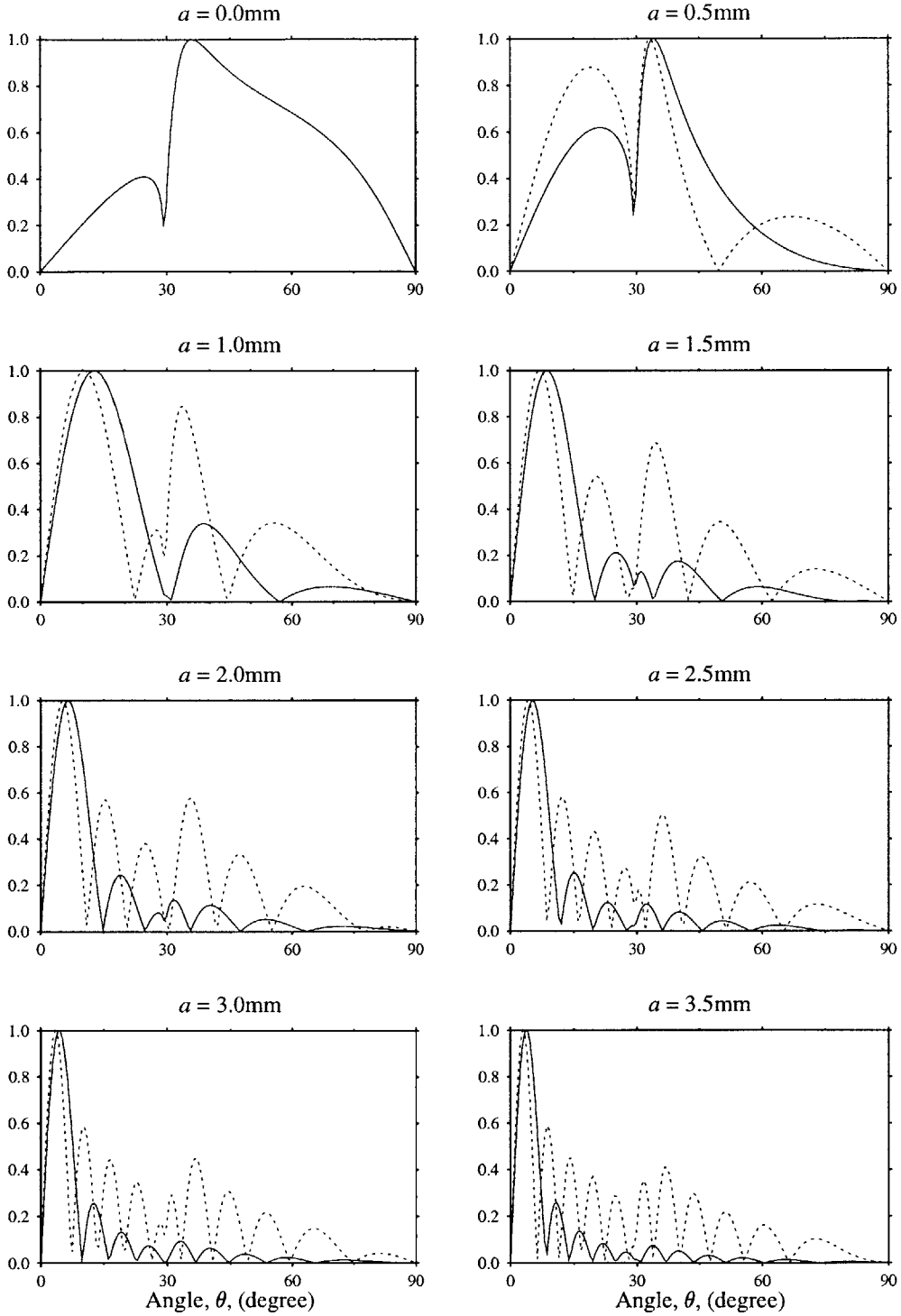

Figure 2-8: Directivities of shear waves from the two models at 5 MHz and various a: solid line represents the elliptical distribution model and dash line the constant loading model.

2.4.4 The Comparison of the Two Models

The difference between the directivities of the two models is that the directivity of the constant loading model consists of the first order Bessel function, whereas that of the new model consists of the second order Bessel function. In order to show the difference clearly, we denote

$$\gamma_1^L = \frac{J_1(k_L a \sin\theta)}{k_L a \sin\theta} \quad \text{and} \quad \gamma_2^L = \frac{J_2(k_L a \sin\theta)}{k_L^2 a^2 \sin^2\theta} \tag{2.59}$$

for longitudinal waves, and

$$\gamma_1^T = \frac{J_1(k_T a \sin\theta)}{(k_T a \sin\theta)} \quad \text{and} \quad \gamma_2^T = \frac{J_2(k_T a \sin\theta)}{(k_T^2 a^2 \sin^2\theta)} \tag{2.60}$$

for shear waves. From Eqs. (2.51), (2.52), (2.46) and (2.47), it can be observed for $\theta = 0°$ that the longitudinal and shear displacements of Case I are exactly four times greater than those of Case II. It can also be observed that the maximum of γ_1^L, γ_2^L, γ_1^T, γ_2^T occur at $\theta = 0°$. In order to make a fair comparison, it is necessary to use the same displacement magnitudes at $\theta = 0°$ for both cases. To do this, we introduce the ratios

$$\gamma^L = \frac{4\gamma_2^L}{\gamma_1^L} \quad \text{and} \quad \gamma^T = \frac{4\gamma_2^T}{\gamma_1^T} \,. \tag{2.61}$$

Figure 2-9 shows the ratio γ^L as the function of θ in aluminum for various a and frequencies. It can be observed from these curves that, for a larger a and larger frequency, γ^L changes more significantly than that of smaller a. γ^T is plotted as the function of angle θ for various a and frequency in Fig. 2-10. It shows that,at large a and high frequency, γ^T changes dramatically and more sharp side lobes appear.

To see the deviation of the two models more clearly, we define

$$\epsilon_a^L = \mid 4\gamma_2^L - \gamma_1^L \mid \quad \text{and} \quad \epsilon_a^T = \mid 4\gamma_2^T - \gamma_1^T \mid \tag{2.62}$$

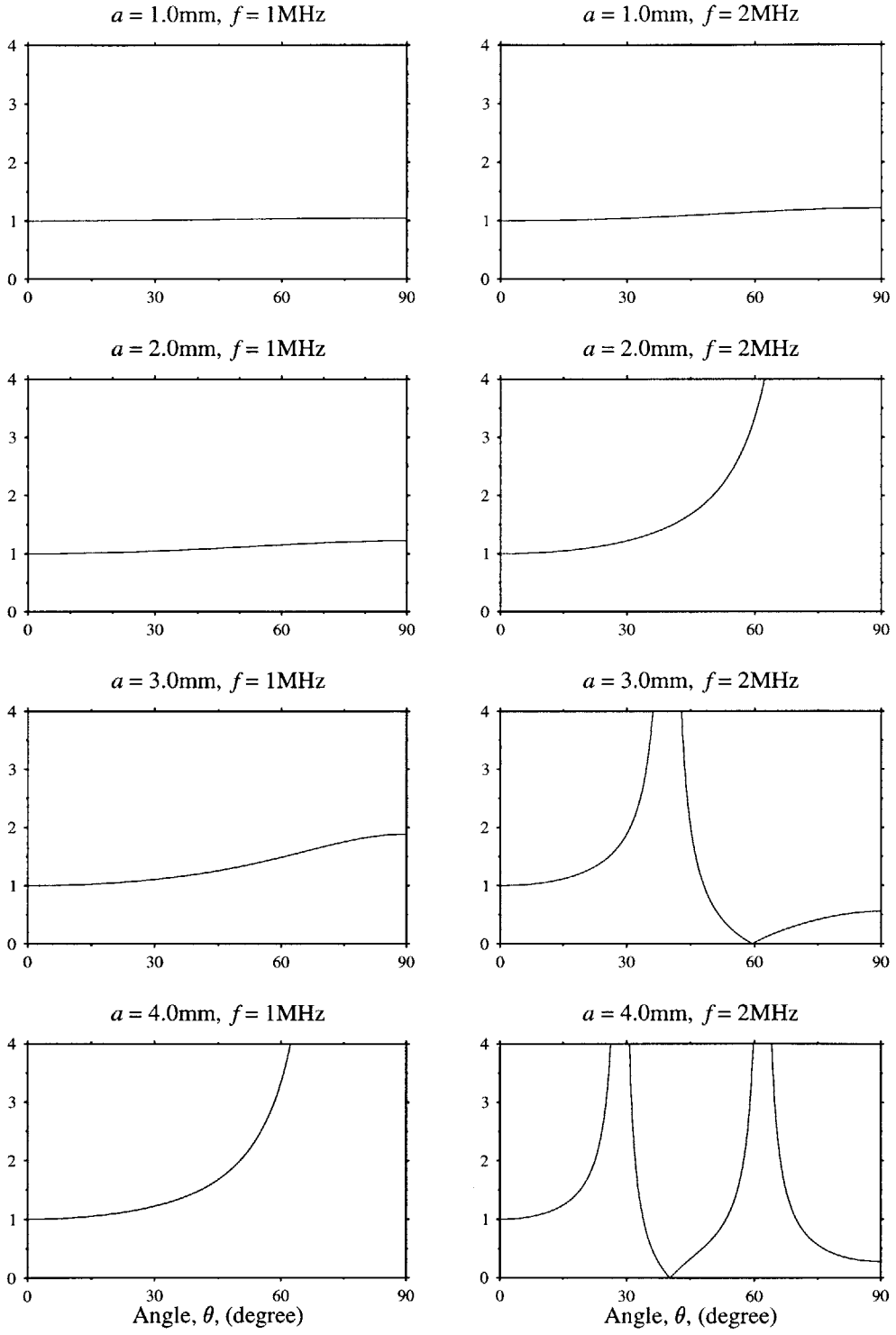

Figure 2-9: The ratio γ^L as the function of θ in aluminum for various a and frequencies.

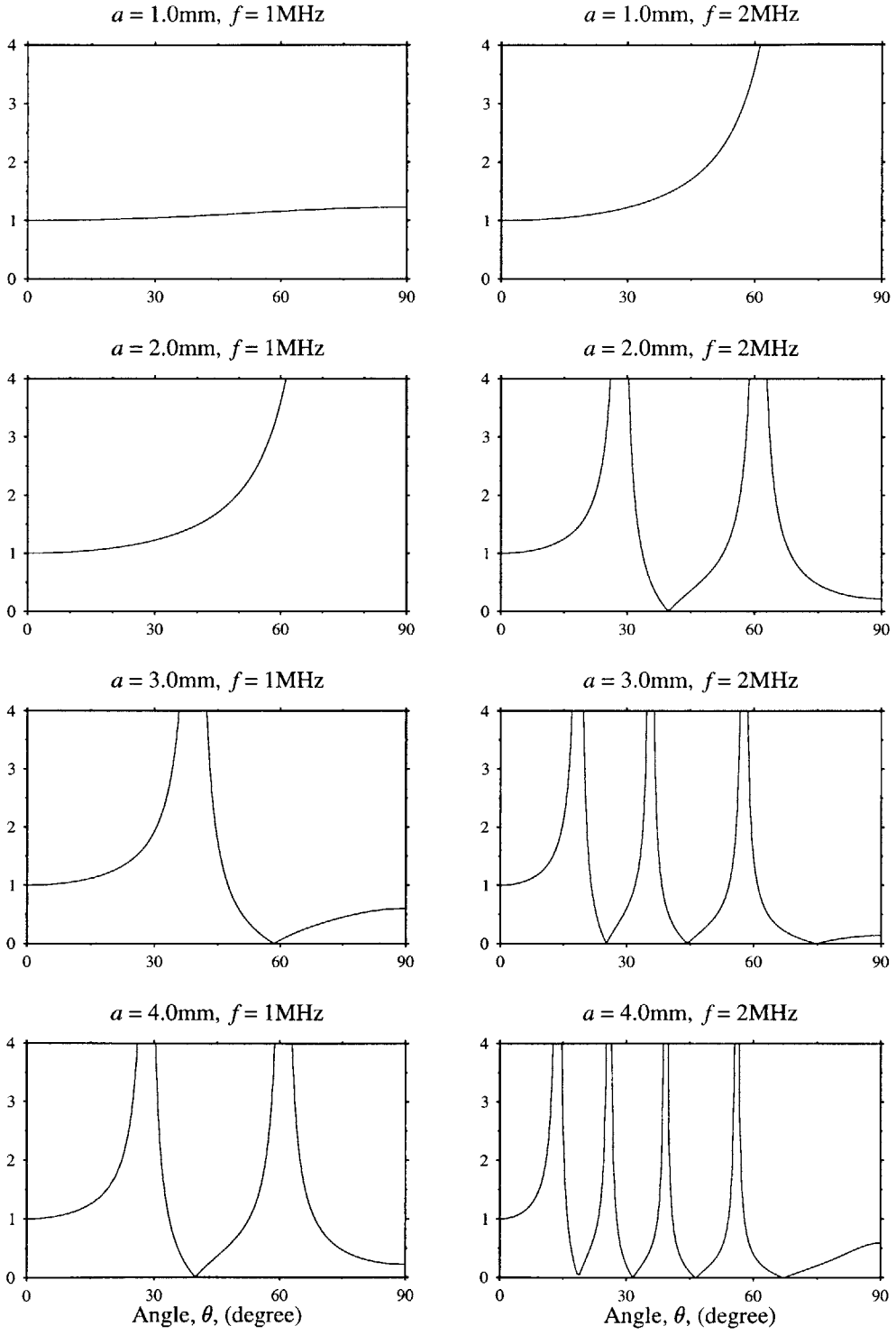

Figure 2-10: The ratio γ^T as the function of θ in aluminum for various a and frequencies.

as the absolute deviation. See Figs. 2-11 and 2-12 for ϵ_a^L and ϵ_a^T, respectively, for various a and frequencies. Similarly, define

$$\epsilon_r^L = \mid 1 - \gamma^L \mid \quad \text{and} \quad \epsilon_r^T = \mid 1 - \gamma^T \mid \tag{2.63}$$

as the relative deviation. The corresponding plots are shown in Fig. 2-13 and 2-14 as the functions of angle θ for various a and frequencies. The plots show that, at small a and low frequency, ϵ^L and ϵ^T changes lightly when angle θ varies, but at larger a and higher frequency, more and more sharp side lobes appear at certain angles indicating that ϵ^L and ϵ^T is changing significantly. This phenomenon shows that the difference between the two models is becoming more significant at large a and high frequency.

The cumulative absolute deviations are defined as

$$\bar{\epsilon}_a^L = \int_0^{\frac{\pi}{2}} \epsilon_a^L d\theta \quad \text{and} \quad \bar{\epsilon}_a^T = \int_0^{\frac{\pi}{2}} \epsilon_a^T d\theta \; . \tag{2.64}$$

and shown in Fig. 2-15 as a function of a at different frequencies. The cumulative relative deviations are defined as

$$\bar{\epsilon}_r^L = \int_0^{\frac{\pi}{2}} \mid 4\gamma_2^L - \gamma_1^L \mid d\theta \quad \text{and} \quad \bar{\epsilon}_r^T = \int_0^{\frac{\pi}{2}} \mid 4\gamma_2^T - \gamma_1^T \mid d\theta \; . \tag{2.65}$$

Figure 2-16 shows the curves of $\bar{\epsilon}$ as the function of a and f.

2.5 Line source excited by normal stresses (width = $2a$)

Line source is another important acoustic sources generated by laser radiation. It is known that the directivity patterns of line sources are different from those of circular sources. Therefore, we present the directivity analysis for the elliptical distribution model for line sources in this section.

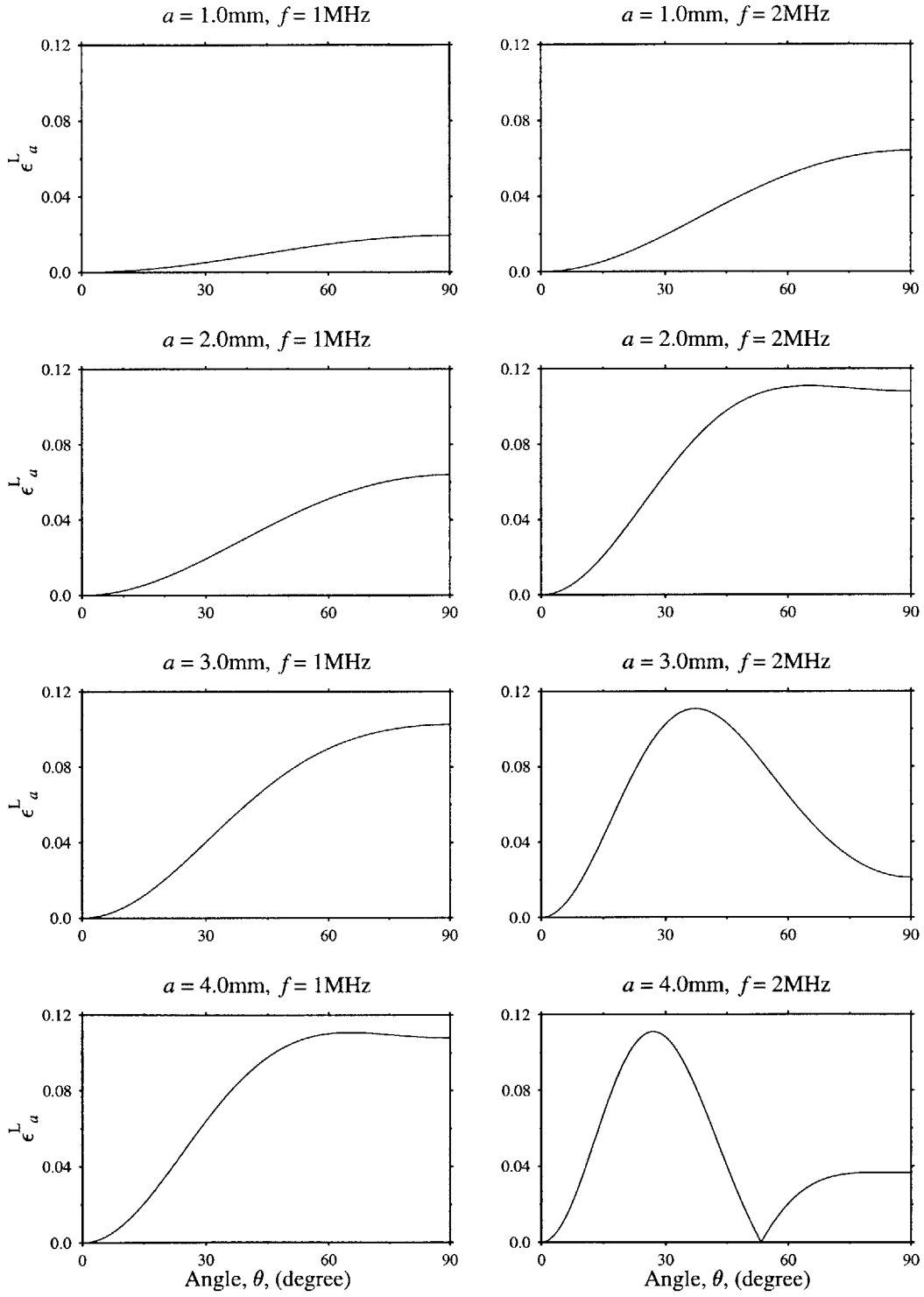

Figure 2-11: The relative difference ϵ_a^L as the function of θ in aluminum for various a and frequencies.

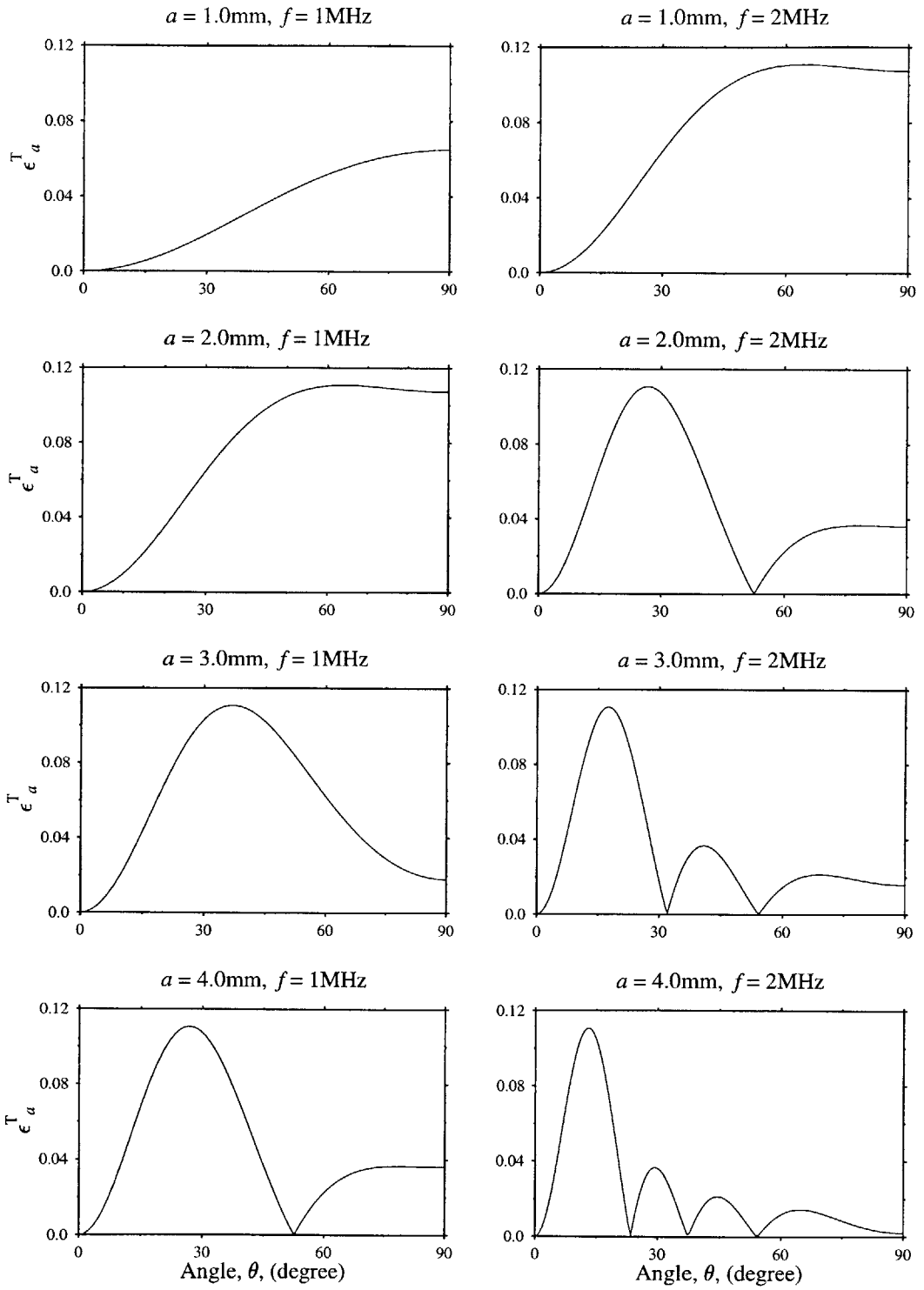

Figure 2-12: The relative difference ϵ_a^T as the function of θ in aluminum for various a and frequencies.

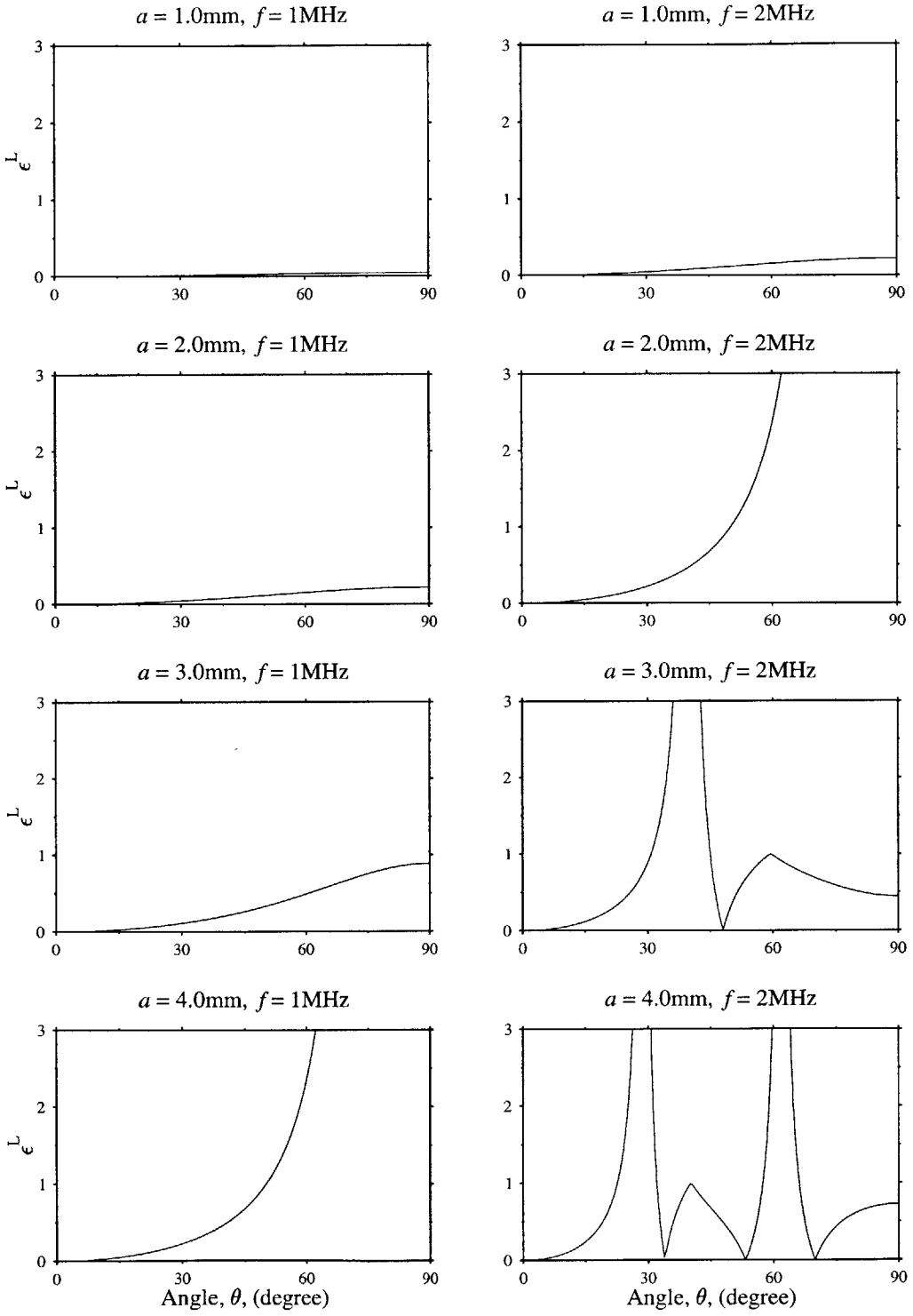

Figure 2-13: The relative difference ϵ_r^L as the function of θ in aluminum for various a and frequencies.

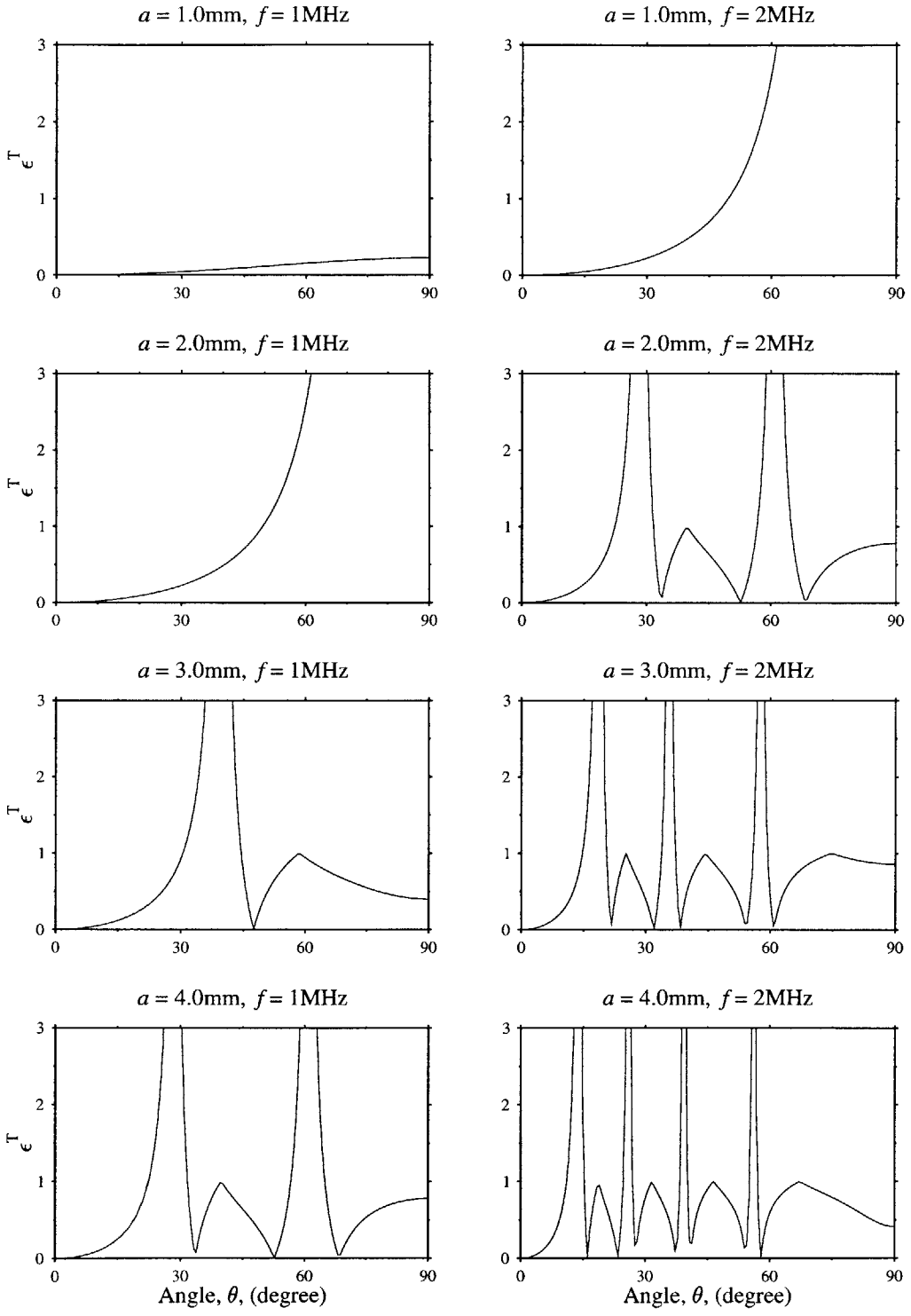

Figure 2-14: The relative difference ϵ_r^T as the function of θ in aluminum for various a and frequencies.

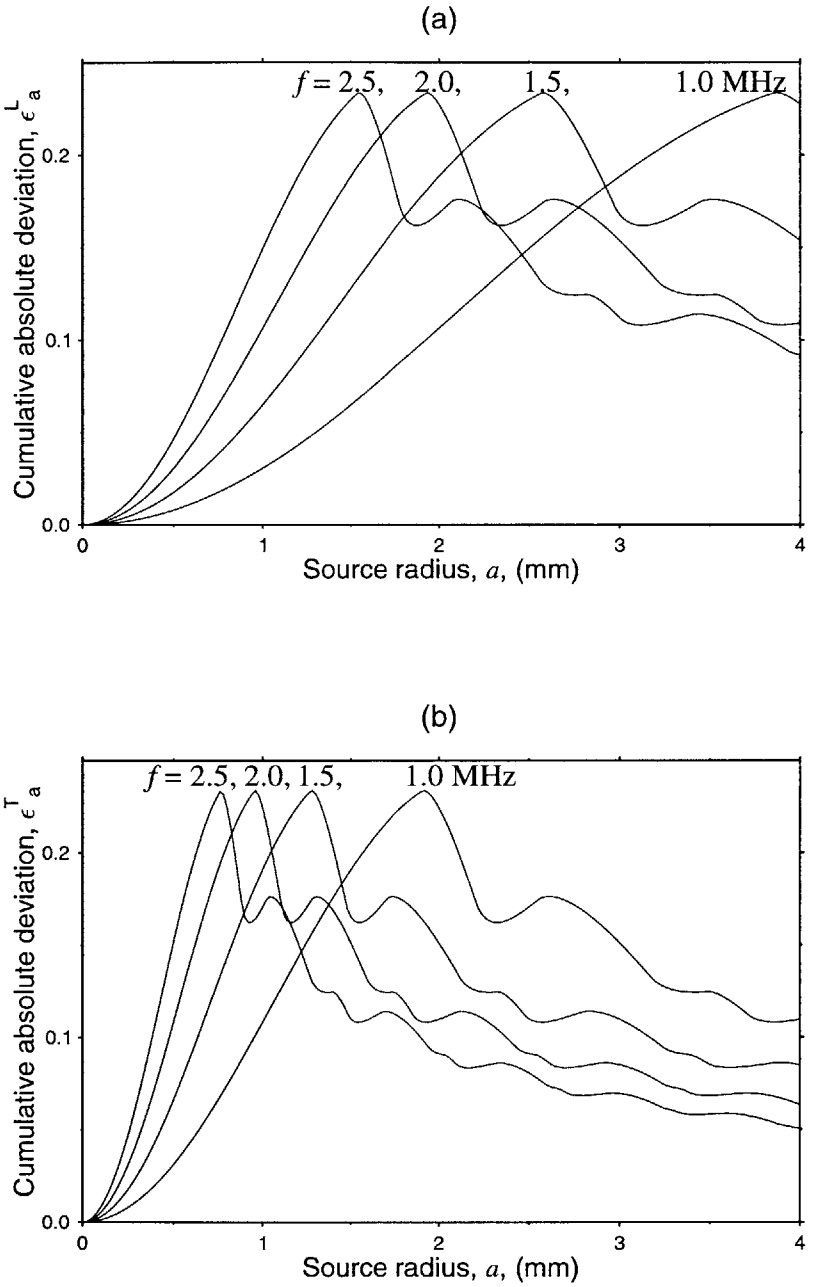

Figure 2-15: The cumulative absolute deviation $\bar{\epsilon}_a$ as the function of a and f in aluminum: (a) longitudinal wave, (b) shear wave.

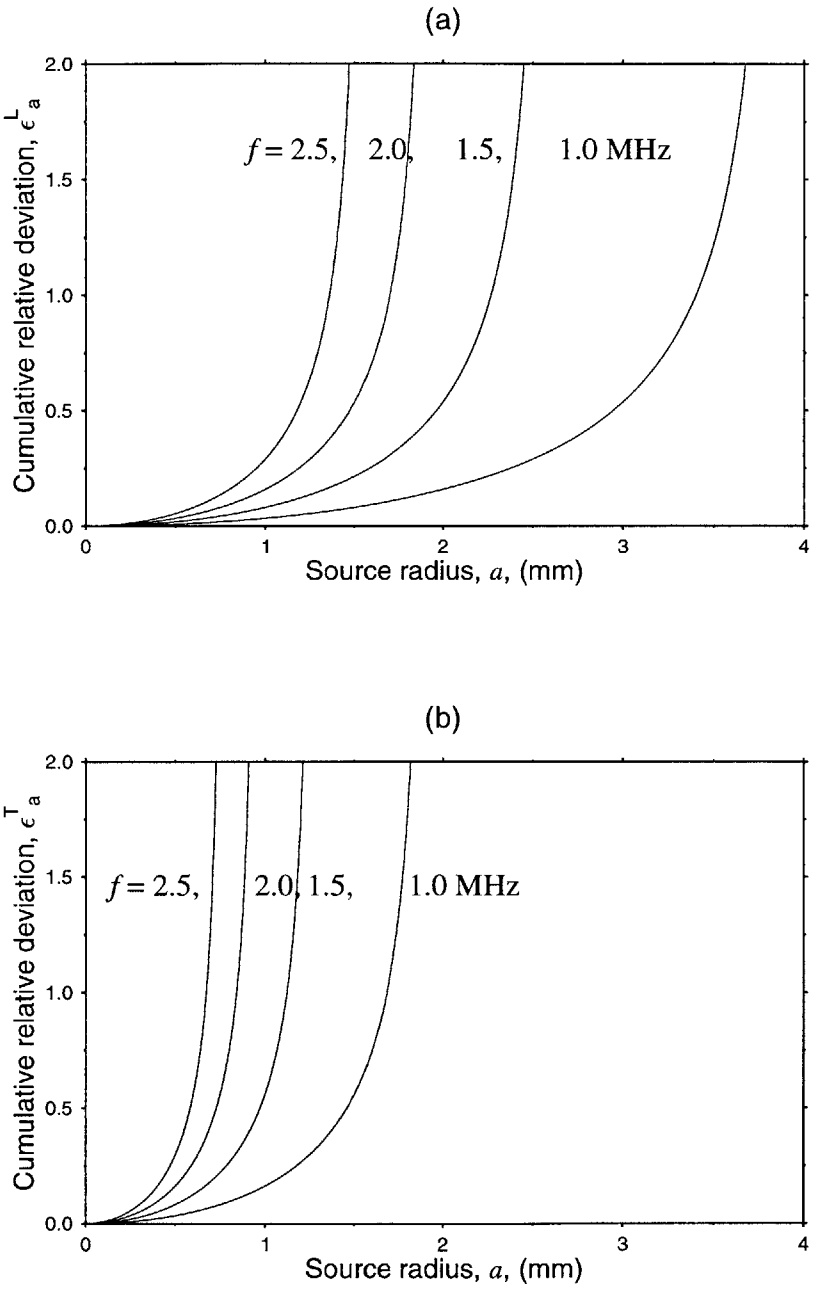

Figure 2-16: The cumulative relative deviation $\bar{\epsilon}_r$ as the function of a and f in aluminum: (a) longitudinal wave, (b) shear wave.

Similar to the circular source, line source is also considered for the difference between the two cases: constant loading (case I) and elliptical loading (case II). Case II is first derived using the Fourier transform and asymptotic method.

2.5.1 The elliptical distribution model

The difference between circular and line sources lies in the distribution of the produced waves. Circular sources produce waves with spherical symmetry, while line sources produce two-dimensional waves with cylindrical symmetry. Therefore, the wave propagation equation for line sources is solved in Cartesian coordinates (x, y, z), with the z-axis normal to the surface and x-axis normal to the axis of the line strip. u_y becomes zero due to the uniform loading along the y-axis, and therefore all the derivatives with the respect to y vanish.

Following the same procedure for the circular source, we obtain

$$\triangle = \boldsymbol{\nabla} \cdot \mathbf{u} = \frac{\partial(u_x)}{\partial x} + \frac{\partial u_z}{\partial z} , \tag{2.66}$$

$$W\mathbf{i}_y = \boldsymbol{\nabla} \times \mathbf{u} = \left(\frac{\partial u_x}{\partial z} - \frac{\partial u_z}{\partial x} \right) \mathbf{i}_y . \tag{2.67}$$

Then the wave propagation equation becomes

$$(\lambda + 2\mu)\frac{\partial \triangle}{\partial x} + \mu \frac{\partial W}{\partial z} + \rho\omega^2 u_x = 0 , \tag{2.68}$$

$$(\lambda + 2\mu)\frac{\partial \triangle}{\partial z} - \mu \frac{\partial(W)}{\partial x} + \rho\omega^2 u_z = 0 , \tag{2.69}$$

so that

$$\frac{\partial^2 \triangle}{\partial x^2} + \frac{\partial^2 \triangle}{\partial z^2} + k_L^2 \triangle = 0 \,, \tag{2.70}$$

$$\frac{\partial^2 W}{\partial x^2} + \frac{\partial^2 W}{\partial z^2} + k_T^2 W = 0 \,. \tag{2.71}$$

The stress boundary conditions are

$$\sigma_{zz} = \lambda \triangle + 2\mu \frac{\partial u_z}{\partial z} \,, \tag{2.72}$$

$$\sigma_{yz} = \mu \left(\frac{\partial u_y}{\partial z} + \frac{\partial u_z}{\partial y} \right) = 0 \,, \tag{2.73}$$

$$\sigma_{zx} = \mu \left(\frac{\partial u_z}{\partial x} + \frac{\partial u_x}{\partial z} \right) \,, \tag{2.74}$$

or can be expressed in terms of the potentials as

$$\frac{\rho \omega^2}{\mu^2} \sigma_{zz} = 2 \frac{\partial^2 W}{\partial x \partial z} - \frac{k_T^2 (k_T^2 - 2k_L^2)}{k_L^4} \frac{\partial^2 \triangle}{\partial x^2} - \left(\frac{k_T}{k_L} \right)^4 \frac{\partial^2 \triangle}{\partial z^2} \,, \tag{2.75}$$

$$\frac{\rho \omega^2}{\mu^2} \sigma_{zx} = \frac{\partial^2 W}{\partial x^2} - \frac{\partial^2 W}{\partial z^2} - 2 \left(\frac{k_T}{k_L} \right)^2 \frac{\partial^2 \triangle}{\partial x \partial z} \,. \tag{2.76}$$

Now Fourier transform is used to eliminate x from these equations. The Fourier transform of a function $f(x)$ and its inverse transform are commonly defined as

$$\hat{f}(\zeta) = \int_{-\infty}^{\infty} f(x) e^{-j\zeta x} dx \,, \tag{2.77}$$

$$f(x) = \frac{1}{2\pi}\int_{-\infty}^{\infty} \hat{f}(\zeta)e^{j\zeta x}d\zeta \ . \tag{2.78}$$

So the Fourier transform of the boundary condition (2.4) is obtained as

$$\hat{\sigma}_{zz} = \frac{4b}{a^2\zeta^3}(\sin\zeta a - a\zeta\cos\zeta a) \ . \tag{2.79}$$

By performing Fourier transform on Eqs. (2.68), (2.69), (2.70), (2.71), (2.75) and (2.76), the Fourier transforms of the potentials are obtained as

$$\hat{\triangle} = \frac{4b\rho\omega^2 k_L^2(k_T^2 - 2\zeta^2)}{a^2\mu^2 k_T^2\zeta^3 G(\zeta)}(\sin\zeta a - a\zeta\cos\zeta a)e^{-z\sqrt{\zeta^2-k_L^2}} \ , \tag{2.80}$$

and

$$\hat{W} = -\frac{8b\rho\omega^2\sqrt{\zeta^2 - k_L^2}}{a^2\mu^2\zeta^2 G(\zeta)}(\sin\zeta a - a\zeta\cos\zeta a)e^{-z\sqrt{\zeta^2-k_T^2}} \ . \tag{2.81}$$

So that the transforms of the displacement components are

$$\hat{u}_z = \frac{4b\sqrt{\zeta^2 - k_L^2}}{a^2\mu\zeta^3 G(\zeta)}(\sin\zeta a - a\zeta\cos\zeta a)\left\{2\zeta^2 e^{-z\sqrt{\zeta^2-k_T^2}} + (k_T^2 - 2\zeta^2)e^{-z\sqrt{\zeta^2-k_L^2}}\right\} \ , \tag{2.82}$$

$$\hat{u}_x = \frac{4b}{ja^2\mu\zeta^2 G(\zeta)}(\sin\zeta a - a\zeta\cos\zeta a)\left\{2\sqrt{(\zeta^2 - k_L^2)(\zeta^2 - k_T^2)}e^{-z\sqrt{\zeta^2-k_T^2}} + (k_T^2 - 2\zeta^2)e^{-z\sqrt{\zeta^2-k_L^2}}\right\} \ . \tag{2.83}$$

Applying the inverse Fourier transform to the above equations, we can obtain the displacement components as

$$u_z = \frac{1}{2\pi}\int_{-\infty}^{\infty} \hat{u}_z e^{j\zeta x}d\zeta \ , \tag{2.84}$$

$$u_x = \frac{1}{2\pi}\int_{-\infty}^{\infty} \hat{u}_x e^{j\zeta x} d\zeta \ , \tag{2.85}$$

The integration in these equations can be evaluated using the asymptotic method which is described in the previous section. The displacements are then obtained as

$$u_z = \frac{2be^{j\frac{\pi}{4}}\cos\theta}{a\mu}\sqrt{\frac{2}{\pi r}}\left\{\frac{2k_T^{\frac{1}{2}}\sqrt{k_T^2\sin^2\theta - k_L^2}}{G(k_T\sin\theta)}\left(\frac{\sin(k_T a\sin\theta)}{k_T a\sin\theta} - \cos(k_T a\sin\theta)\right)e^{-jk_T r}\right.$$
$$\left. + \frac{jk_T^{-\frac{1}{2}}\cos\theta(k_T^2 - 2k_L^2\sin^2\theta)}{\sin^2\theta G(k_L\sin\theta)}\left(\frac{\sin(k_L a\sin\theta)}{k_L a\sin\theta} - \cos(k_L a\sin\theta)\right)e^{-jk_L r}\right\} , \tag{2.86}$$

$$u_x = \frac{2be^{j\frac{\pi}{4}}\cos\theta}{a\mu}\sqrt{\frac{2}{\pi r}}\left\{\frac{2k_T^{\frac{1}{2}}\cos\theta\sqrt{k_T^2\sin^2\theta - k_L^2}}{\sin\theta G(k_T\sin\theta)}\left(-\frac{\sin(k_T a\sin\theta)}{k_T a\sin\theta} + \cos(k_T a\sin\theta)\right)e^{-jk_T r}\right.$$
$$\left. + \frac{jk_T^{-\frac{1}{2}}(k_T^2 - 2k_L^2\sin^2\theta)}{\sin\theta G(k_L\sin\theta)}\left(\frac{\sin(k_L a\sin\theta)}{k_L a\sin\theta} - \cos(k_L a\sin\theta)\right)e^{-jk_L r}\right\} , \tag{2.87}$$

By using the relation

$$U_{la}^L = u_z\cos\theta + u_x\sin\theta \ , \tag{2.88}$$

$$U_{la}^T = u_x\cos\theta - u_z\sin\theta \ , \tag{2.89}$$

and the notation in Eqs. (2.48), the radial and tangential displacement components of the field are obtained as

$$U_{la}^L(r,\theta) = \left(\frac{2ab}{\mu}\right)e^{i\left(\frac{3\pi}{4} - k_L r\right)}\sqrt{\frac{2}{\pi r k_L}}\frac{1}{\xi_L^2}\left(\frac{\sin(\xi_L)}{\xi_L} - \cos(\xi_L)\right)U_0^L(\theta) \ , \tag{2.90}$$

$$U_{la}^{T}(r,\theta) = \left(\frac{2ab}{\mu}\right) e^{i\left(\frac{5\pi}{4}-k_T r\right)} \sqrt{\frac{2}{\pi r k_T}} \frac{1}{\xi_T^2} \left(\frac{\sin(\xi_T)}{\xi_T} - \cos(\xi_T)\right) U_0^T(\theta) \ , \tag{2.91}$$

where $U_0^L(\theta)$ and $U_0^L(\theta)$ are the far-field amplitudes of the compression wave radiated from a point source, as shown in Eqs. (2.49) and (2.50).

2.5.2 The constant loading model

For the case of constant loading, the displacement amplitudes of the longitudinal and shear waves are derived as [6]

$$U_{la}^{L}(r,\theta) = \frac{ab}{\mu} e^{i\left(\frac{3\pi}{4}-k_L r\right)} \sqrt{\frac{2}{\pi r k_L}} \frac{\sin(\xi_L)}{\xi_L} U_0^L(\theta) \ , \tag{2.92}$$

$$U_{la}^{T}(r,\theta) = \frac{ab}{\mu} e^{i\left(\frac{5\pi}{4}-k_T r\right)} \sqrt{\frac{2}{\pi r k_T}} \frac{\sin(\xi_T)}{\xi_T} U_0^T(\theta) \ . \tag{2.93}$$

2.5.3 Directivity patterns of the two cases

Still the displacements of the two models for the line source show the similar patterns except for the modification terms: $\dfrac{\sin(\xi_T)}{\xi_T}$ and $\dfrac{1}{\xi_L^2}\left(\dfrac{\sin(\xi_L)}{\xi_L} - \cos(\xi_L)\right)$. To see the difference, the displacements U_{la}^L and U_{la}^T are normalized and the far-field directivities are then obtained as

$$H_{la1}^{L}(\theta) = \frac{\sin(\xi_L)}{\sin\theta} H_0^L(\theta) \ , \tag{2.94}$$

$$H_{la1}^{T}(\theta) = \frac{\sin(\xi_T)}{\sin\theta} H_0^T(\theta) \tag{2.95}$$

for Case I, and

$$H_{la2}^{L}(\theta) = \frac{1}{\sin^2\theta}\left(\frac{\sin(\xi_L)}{\xi_L} - \cos(\xi_L)\right) H_0^L(\theta) \ , \tag{2.96}$$

$$H_{la2}^{T}(\theta) = \frac{1}{\sin^2\theta}\left(\frac{\sin(\xi_T)}{\xi_T} - \cos(\xi_T)\right) H_0^T(\theta) \tag{2.97}$$

for Case II, where $H_0^L(\theta)$ and $H_0^T(\theta)$ are the far-field directivities of point sources shown in Eqs. (2.57) and (2.58).

The directivity patterns for the two cases are plotted for various a and certain frequencies, as shown in Figs. 2-17 and and 2-18 for the directivities at various a and 1 MHz frequency, and Figs. 2-19 and and 2-20 at 5 MHz frequency. The difference between the two models for the line source is clearly shown in the directivity plots. The trend is similar to the case of circular source: the difference increases between the two models when the width of laser line source $2a$ increases, and when frequency increases. ,

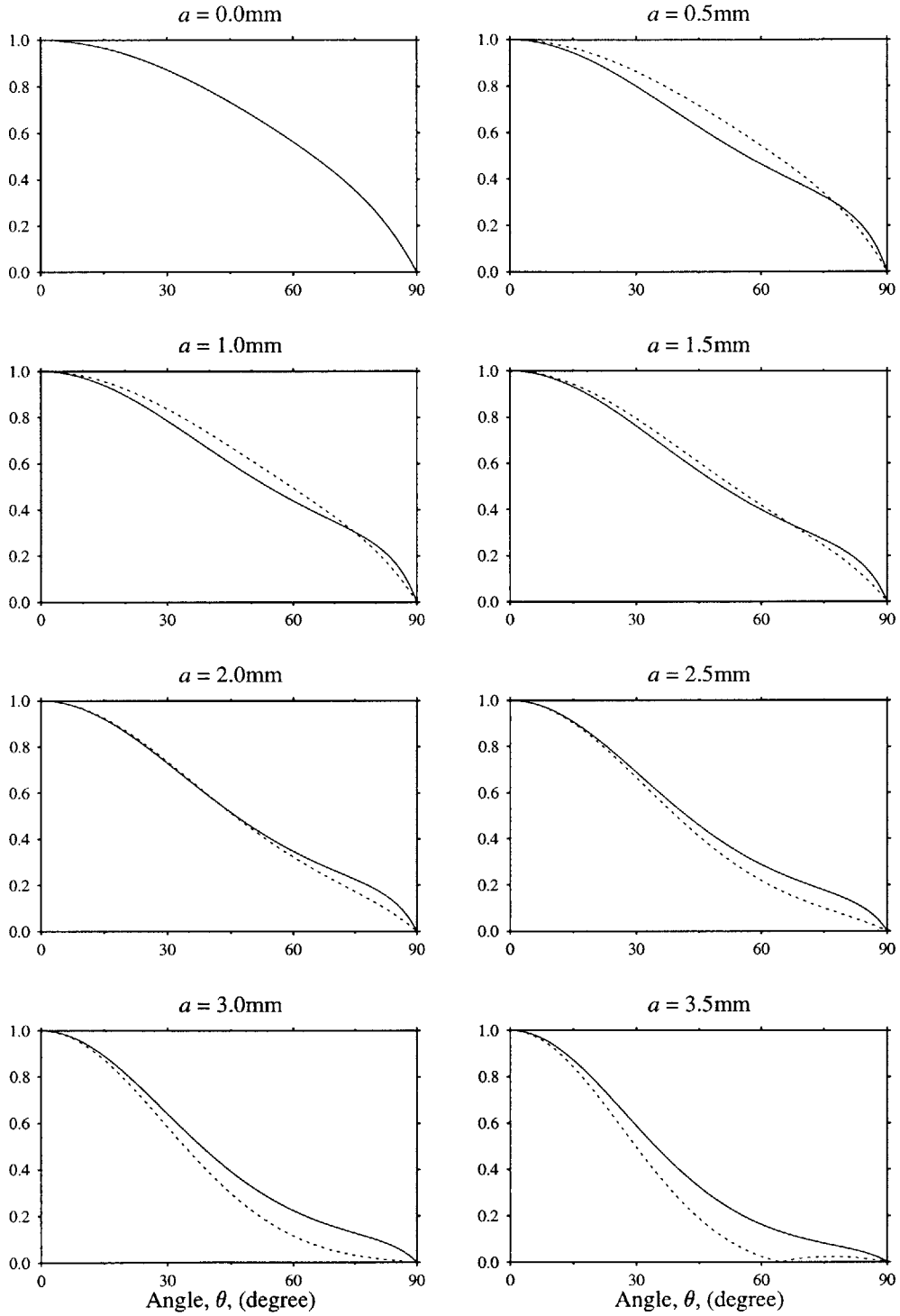

Figure 2-17: Directivities of longitudinal waves for line source at 1 MHz and various a: solid line represents the elliptical distribution model and dashed line the constant loading model.

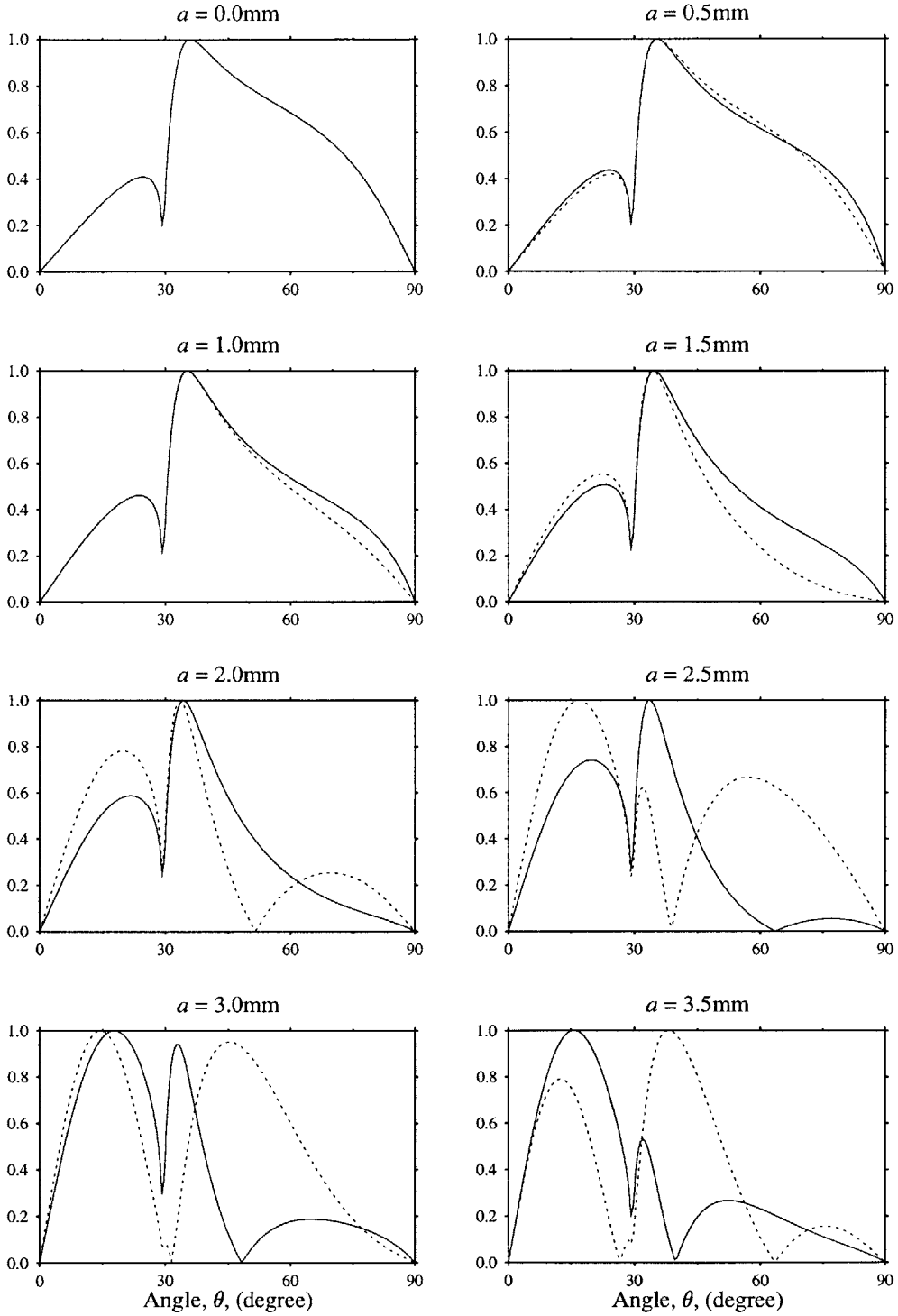

Figure 2-18: Directivities of shear waves for line source at 1 MHz and various a: solid line represents the elliptical distribution model and dash line the constant loading model.

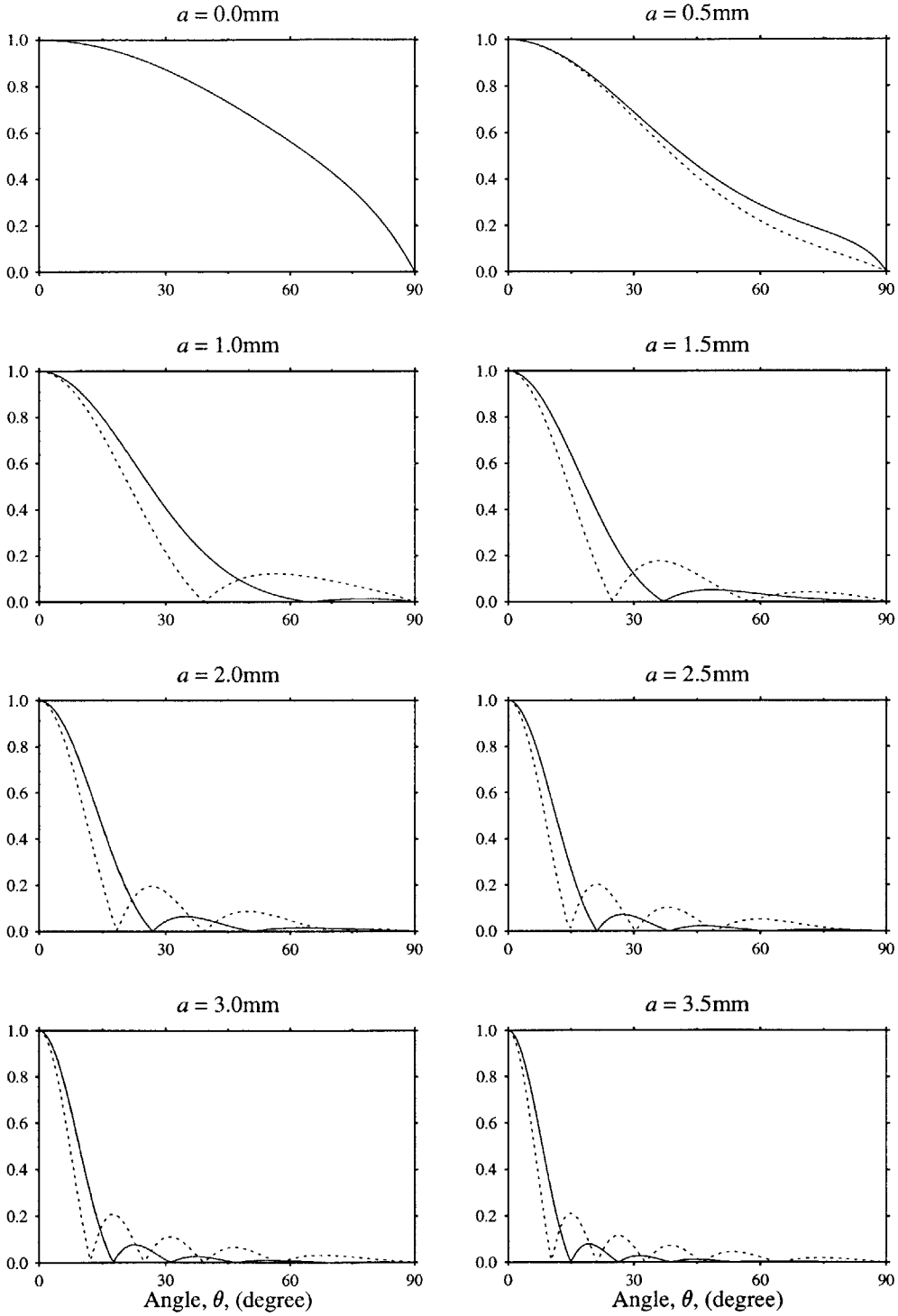

Figure 2-19: Directivities of longitudinal waves for line source at 5 MHz and various a: solid line represents the elliptical distribution model and dashed line the constant loading model.

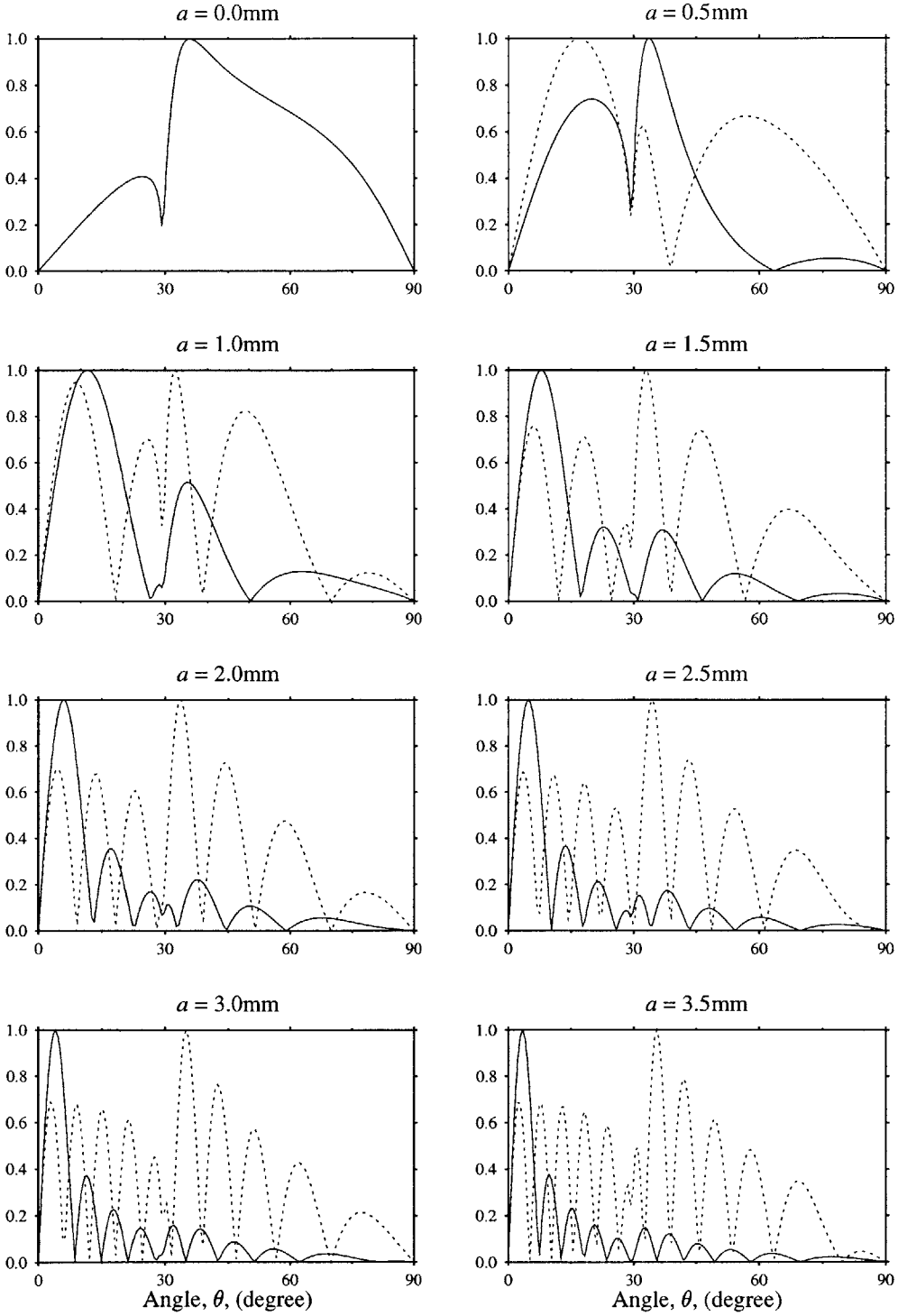

Figure 2-20: Directivities of shear waves for line source at 5 MHz and various a: solid line represents the elliptical distribution model and dash line the constant loading model.

Chapter 3

Experimental Directivity Measurements

This chapter discusses several directivity measurements on an aluminum standard specimen under different laser radiations. The directivity of an acoustic source can be experimentally obtained by measuring the displacements at different propagation angles, and plotting them as a function of angle θ. A high-power pulsed laser is used to generated ultrasound in the sample. Two types of reception sensors are used. A high-power continuous wave (cw) laser system detects the surface displacements induced by the laser-generated ultrasound. The other is a PVDF transducer which also measures the surface displacements. The PVDF transducer has a center frequency at 5 MHz, so it is chosen to measure the displacements at a higher frequency. In contrast, the cw laser can only measure the displacement at relatively low frequencies around 1 MHz, due to the usage of the low-pass filter.

The experiments are focused on circular laser sources.

3.1 Beam Propagation Cases

Figure 3-1 shows an acoustic ray propagating at an angle θ in a bounded medium, originated from a laser source point O and observed at a point A on the surface. In solid mediums where both normal and shear stresses can occur simultaneously, both longitudi-

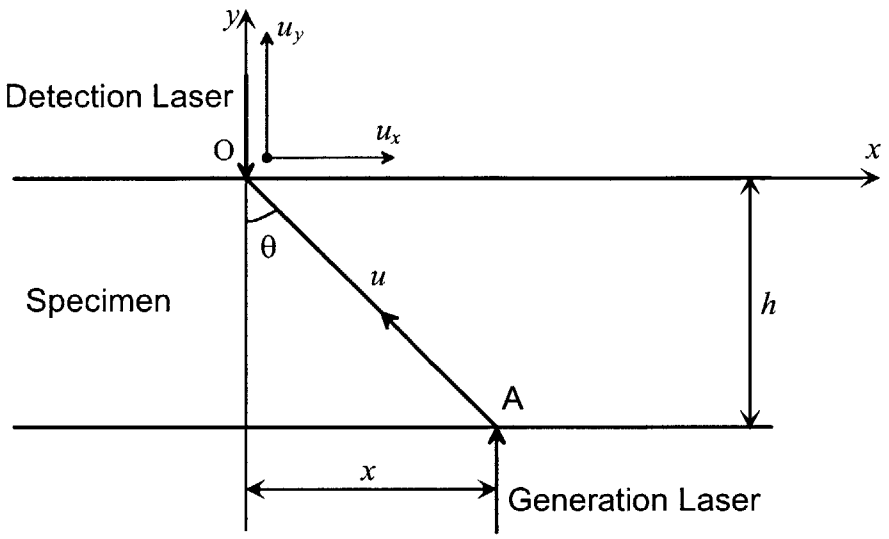

Figure 3-1: An acoustic ray propagating in a bounded medium, originated from a laser source point O and observed at Point A.

nal and shear waves may be propagating in the same direction (at different velocities). In a comprehensive analysis, the conversion of wave modes at the interfaces where an oblique incident wave reflects off could be taken into account. But for simplicity, the preliminary study considers only the simple cases shown in Fig. 3-2.

Neglecting the effects of multiple reflections and mode conversions, four different scenarios should be considered, which include the measurements of: (I) normal displacement of L-wave, (II) normal displacement of T-wave, (III) transverse displacement of L-wave, and (IV) transverse displacement of T-wave at Point A. One of the ways to measure the normal and transverse displacement components is to use longitudinal and shear piezoelectric transducers. However, a laser-based detection system can indicate only the normal displacements so that Scenarios III and IV become out of our concerns. However, for completeness, all four cases are included in the analysis. The corresponding vertical and horizontal components of displacement amplitudes (U_y^L, U_y^T, U_x^L, U_x^T) are written respectively in Fig. 3-2 as a function of the location of observation (x) and the specimen thickness

Case I

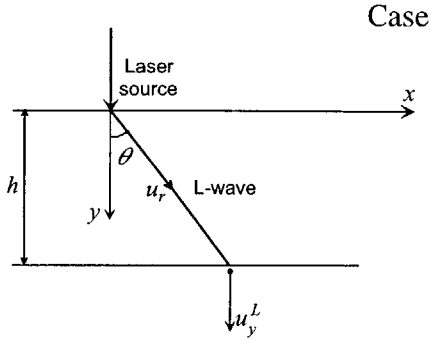

$$U_y^L = U^L \frac{h}{(h^2 + x^2)^{0.5}}$$

Case II

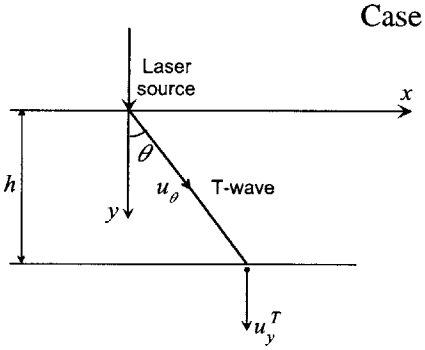

$$U_y^T = U^T \frac{x}{(h^2 + x^2)^{0.5}}$$

Case III

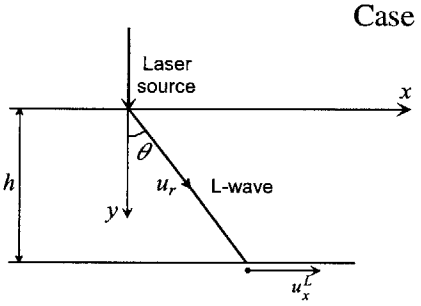

$$U_x^L = U^L \frac{x}{(h^2 + x^2)^{0.5}}$$

Case IV

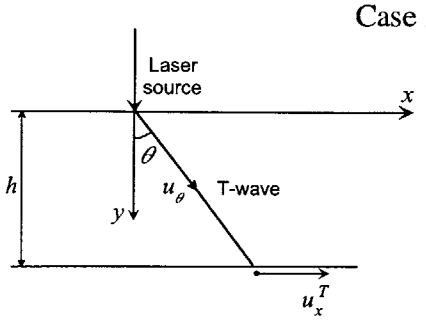

$$U_x^T = U^T \frac{h}{(h^2 + x^2)^{0.5}}$$

Figure 3-2: Four different detection scenarios measuring normal and transverse displacement amplitudes of longitudinal and shear waves traveling at an angle θ.

(h). The displacement amplitudes U^L and U^T can be determined from Section 2 by considering the illumination shape and strength of the laser beam. For example, the normal displacement amplitudes for a circular source of radius a for the elliptical distribution case can be written as

$$U_a^L(r,\theta) = \left(\frac{2a^2b}{\mu}\right)\left(\frac{e^{-jk_Lr}}{r}\right)\left(\frac{J_2(\xi_L)}{\xi_L^2}\right)U_0^L(\theta)\,, \tag{3.1}$$

$$U_a^T(r,\theta) = \left(\frac{2a^2b}{\mu}\right)\left(\frac{e^{-jk_Tr}}{r}\right)\left(\frac{J_2(\xi_T)}{\xi_T^2}\right)U_0^T(\theta)\,, \tag{3.2}$$

and

$$U_a^L(r,\theta) = \left(\frac{a^2b}{\mu}\right)\left(\frac{e^{-jk_Lr}}{r}\right)\left(\frac{J_1(\xi_L)}{\xi_L}\right)U_0^L(\theta)\,, \tag{3.3}$$

$$U_a^T(r,\theta) = \left(\frac{a^2b}{\mu}\right)\left(\frac{e^{-jk_Tr}}{r}\right)\left(\frac{J_1(\xi_T)}{\xi_T}\right)U_0^T(\theta)\,. \tag{3.4}$$

for the constant loading case, respectively.

3.2 Instrumentation

3.2.1 Generation of Ultrasound

- *Pulsed laser*: a New Wave MiniLase laser system is used for generation of ultrasound. The laser type is flash lamp pumped, Q-switched, water cooled, Nd:YAG laser. Table 3.1 shows the specifications of the laser source.

In the experiments, the surface of the specimen is moisturized by water. When the laser beam passes through the water, the water is evaporated within a small region. In

Parameter	*Value*
Wavelength (λ)	1064 nm
Pulse width	6–8 ns
Energy level	90 mJ
Beam diameter ($2a$)	3.75 mm
Maximum pulse repetition rate	10 Hz

Table 3.1: Specifications of the pulsed laser system.

the mean time, a high-amplitude stress wave, usually called shock wave, radiates from the evaporated region. The stress wave acts as the ultrasound source. In this case, the ultrasound is generated by the momentum exchange between the water and the specimen instead of the heat expansion in the specimen itself. So the directivity patterns of laser-generated ultrasound for wet and dry surfaces may be different from each other.

3.2.2 Reception of Ultrasound

- *Continuous wave laser*: a solid-state diode-pumped, frequency-doubled Nd:Vanadate (Nd:YVO_4) cw laser (Verdi V-8) is used to detect the surface displacements on the specimen. Its parameters are specified in Table 3.2.

Parameter	*Value*
Wavelength (λ)	532 nm
Output power	$\leq$ 8 W
Beam diameter ($2a$)	2.25 mm$\pm$10%
Beam divergence	0.35 mrad$\pm$10%

Table 3.2: Specifications of the Verdi V-8 laser system.

A photo-emf detector was installed together with the cw laser to convert the mechanical signals into electrical signals. The principle of the photo-emf detector is based on a reference-beam interferometer with the measurements of the nonsteady state

photo-electromotive force. See Fig. 3-3 for the schematic diagram of photo-emf receiver. The cw laser is first divided, by a beamsplitter, into a reference beam and a probe beam which is directed to the specimen. The light reflecting or scattering from the specimen is then collected as the signal beam and delivered to the photo-emf detector. At the same time, the reference beam is also directed into the detector. If the sample surface is deformed due to an ultrasonic excitation, a phase change will be introduced onto the signal beam. As the result of the interference between the two beams, this phase change induces a transient shift in the lateral position of the fringe pattern on the photo-emf detector. This lateral shift produces an electrical signal that is proportional to the instantaneous surface displacement at ultrasonic frequencies. The surface displacement on the order of 0.1-10 nm can be detected by this detector. Various output gain settings allow the observation of output signals in a convenient voltage range for display on an oscilloscope or for digitizing in an electrical processor.

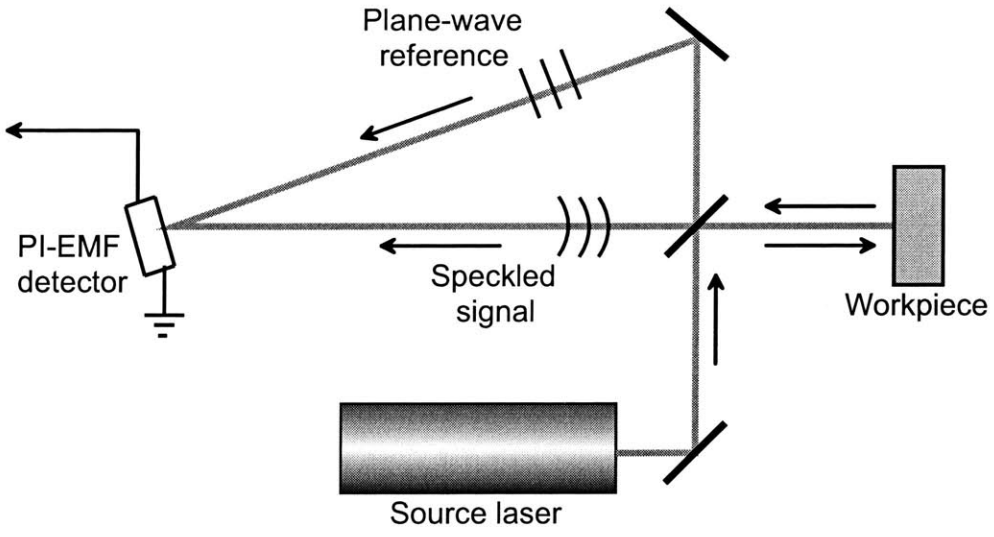

Figure 3-3: The schematic diagram of photo-emf detector.

- *PVDF transducers*: a PVDF transducer with the size of 10mm×10mm is employed to measure the surface displacements of the specimen. PVDF transducer is made from a kind of piezoelectric polymer material, which is a plastic material with groups of molecules linked as orderly crystallites. The crystallites form in an amorphous matrix of chemically similar, but differently structured material. The relative population of crystallites strongly effects the piezoelectric behavior of the material. Polyvinylidene fluoride is a popular piezoelectric polymer material to make sensors.

3.2.3 Other instrument

- Oscilloscope: Tektronix TDS 210 two channel digital oscilloscope is used to record the waveforms. In the experiments, oscilloscope trace is triggered by the laser pulse via external trigger. The selection of resolution depends on the time-of-flight of signals in every experiment.
- Function Generator: HP 33120A function generator / arbitrary waveform generator is used to calibrate the photo-emf detector system.
- Sliding table: the resolution of this table is 0.0254 mm. It provides the measurement of the profile of the surface displacements.
- Plano-convex lens: the effective focal length is 100 mm. This lens is used to focus or enlarge the pulsed laser beam to different sizes.

3.2.4 Specimen

- Aluminum block: 32 mm thick. Figures 3-4(a) and (b) respectively show the waveforms obtained at two different locations x (corresponding to the propagating angle $\theta = 0°$ and 45°). In Fig. 3-4(a), the largest peak appears at $t \approx 5.12\mu s$. This is the longitudinal wave propagating directly in the direction normal to the surface of the specimen. At another angle $\theta = 45°$ (Fig. 3-4(b)), the longitudinal wave arrives at a

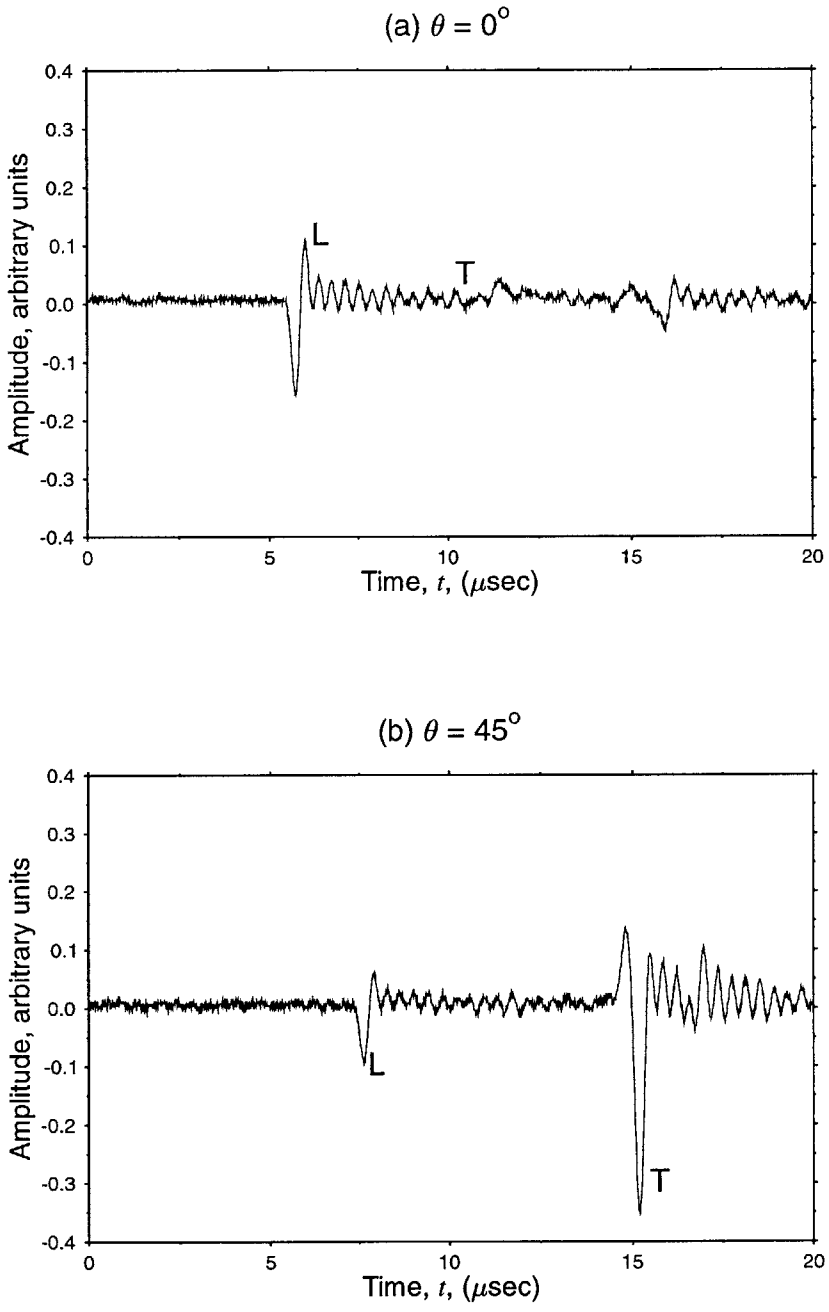

Figure 3-4: Waveforms obtained at two different locations ($\theta = 0°, 45°$) on the aluminum specimen (h = 32 mm).

later time: $t \approx 7.24\mu s$ since this wave travels a longer distance. On the other hand, there is a large peak standing at $t \approx 14.41\mu s$. This is a shear wave propagating at 45°. Note the enormous amplitude of this wave.

By knowing the longitudinal and shear wave speeds $c_L = 6250$ m/s and $c_T = 3140$ m/s, we can precisely predict the arrival times t_L and t_T of each mode. In the experiments, the out-of-plane displacements are measured for different locations and plotted for both modes. The corresponding directivities are computed.

3.3 Experimental Setup

According to the discussion in Sec. 3.1, the experimental setup is installed as shown in Fig. 3-5. The experiments are performed in the following procedure: the Nd:YAG pulsed laser strikes normally at a point A (Fig: 3-1), ultrasound is generated and radiated into the sample. At the same time, the cw laser aiming at a fixed point O on the other side of the surface, or the PVDF transducer attached at O, measures the displacements of the point. By varying the angle of propagation θ, the position of the pulsed laser source is off-centered by the distance x, which is controlled with the sliding table. Specifically, we are only concerned about measuring the out-of-plane displacements U_y introduced by longitudinal and shear waves as:

$$U_y^L = U^L \cos\theta, U_x^L = U^L \sin\theta \tag{3.5}$$

$$U_y^T = U^T \sin\theta, U_x^T = U^T \cos\theta. \tag{3.6}$$

The detected mechanical displacements are then converted to the electrical signals, which is retrieved and shown in the oscilloscope. By measuring the corresponding peak-to-peak amplitude of the longitudinal and shear waves at various angles, the directivities can be constructed. The results are shown and discussed in the next chapter.

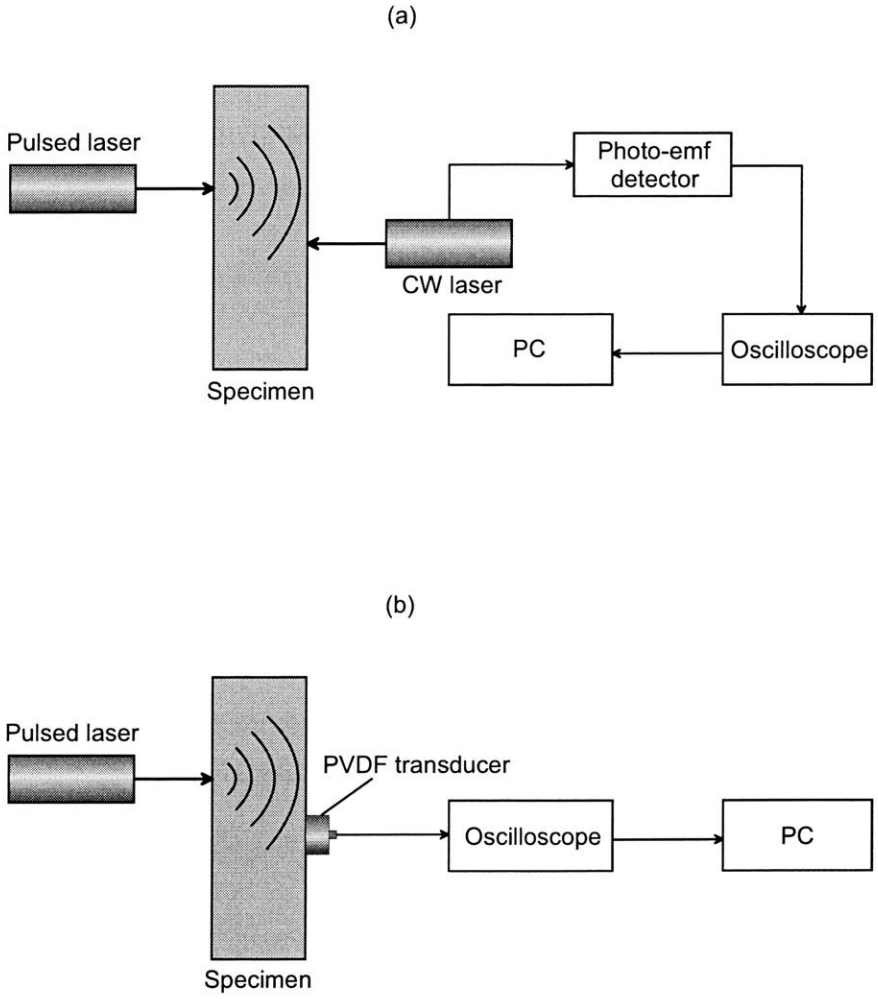

Figure 3-5: The experimental setup for the measurement of displacements: (a) CW laser, (b) PVDF transducer.

3.4 Spectral Analysis

For a signal retrieved with the cw laser system, a representative frequency should be chosen when the outcomes are compared to the theoretical results. This is due to the broad bandwidth of the ultrasound generated by the pulsed laser. Therefore, spectral analysis is carried out on the waveforms prior to the displacement measurements. The signals are retrieved under the condition that the pulsed laser beam was focused to be 1 mm, the sample surface moisturized by water, and several low-pass filters, such as 2, 5 and 10 MHz, are used. The waveforms and the corresponding Fourier transforms are shown in Fig. 3-6, respectively. It is noticed that the center frequency of all the waveforms are around 1 MHz. So 1 MHz is chosen to calculate the theoretical directivity which is then compared to the experimental results.

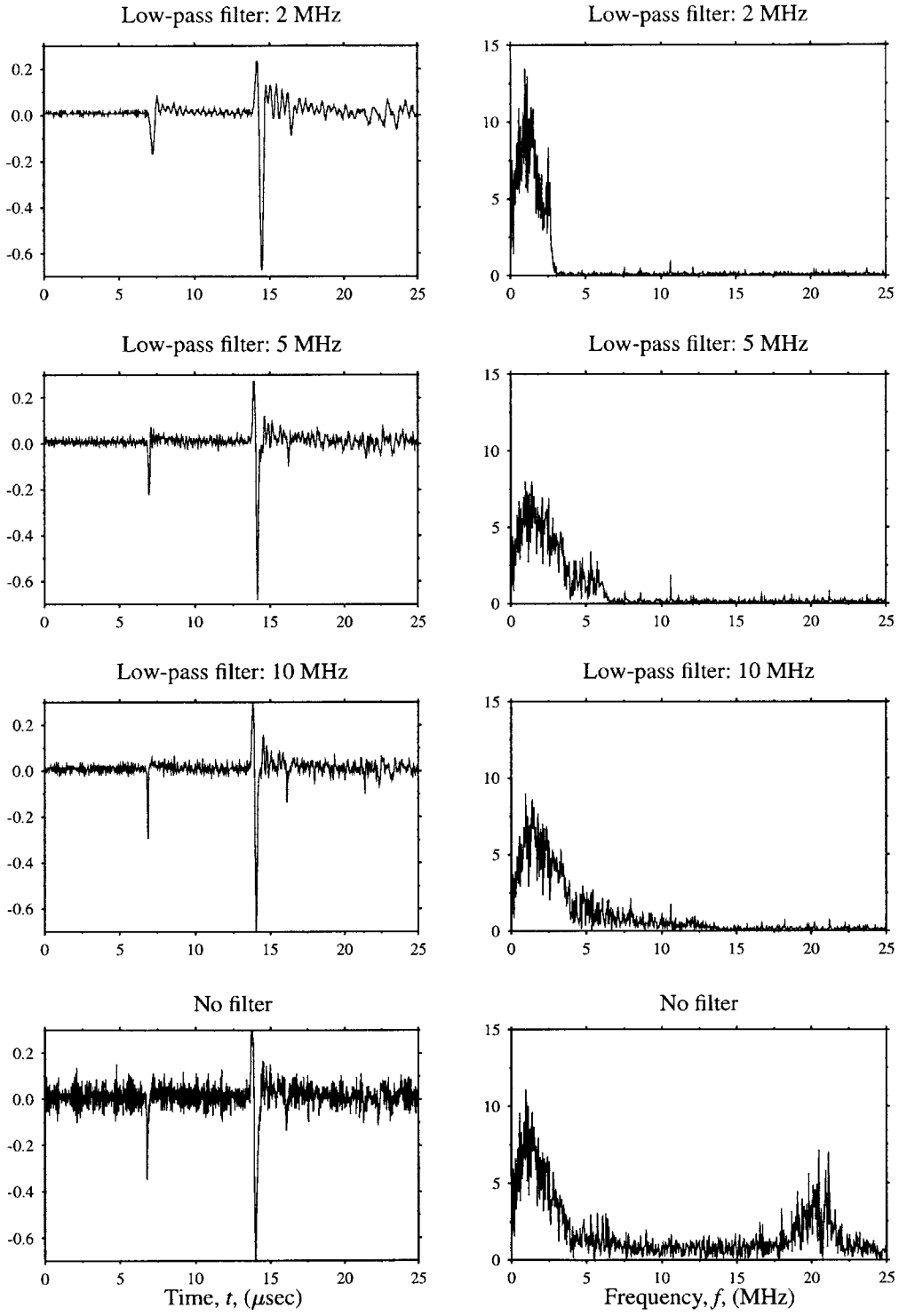

Figure 3-6: The spectral analysis of waveforms retrieved from cw laser.

Chapter 4

Results and discussion

4.1 Experimental results

With the apparatus described in the previous chapter, the ultrasonic directivity patterns at 1 and 5 MHz are determined and compared with the theoretical results. These results are obtained by either the detection laser or PVDF transducers. Under all circumstances, the sample surface on the generation laser side is moderately moistured by water.

First, several experiments are performed to measure the out-of-plane displacements for various pulsed laser beam sizes ($2a$), using the cw laser as the detection sensor. The plots of the measured out-of-plane displacements U_y^L and U_y^T vs. the propagation angle θ are shown in Fig. 4-1 for longitudinal waves, and Fig. 4-2 for shear waves. In these figures and the following directivity plots, solid lines represent theoretical results, and dashed lines show experimental outcomes. The theoretical plots corresponding to the constant loading (case I) are on the left side in the figures, while the plots corresponding to the elliptical loading (case II) are on the right side. According to the spectral analysis introduced in Section 3.4, 1 MHz is chosen as the frequency of interest to determine the theoretical directivity plots. For longitudinal waves, the out-of-plane displacements reaches the maximum at $\theta = 0°$ for all chosen a, and then monotonously drops while the propagation angle θ increases.

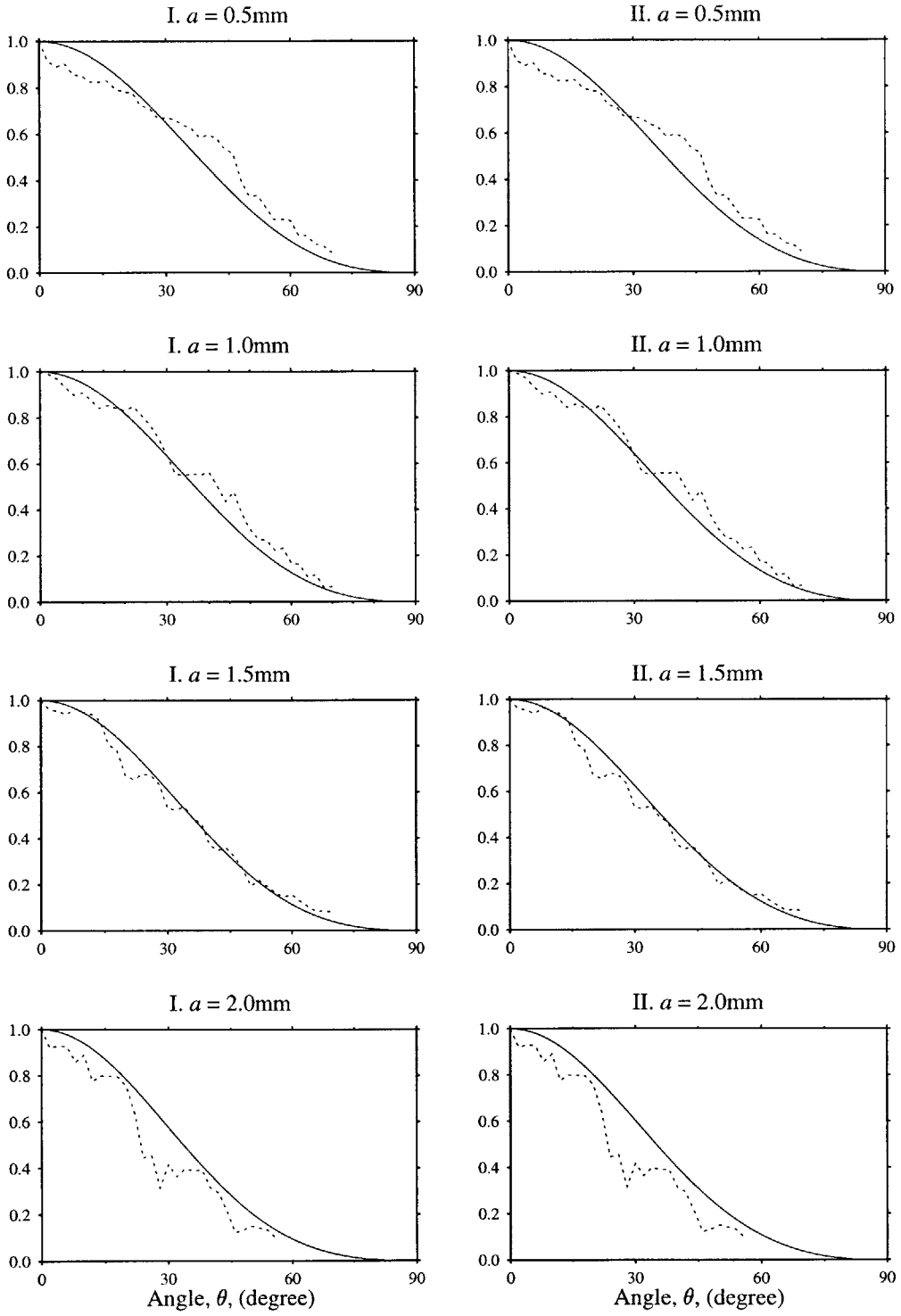

Figure 4-1: The measured out-of-plane displacements (U_y^L) as a function of propagating angle θ for the aluminum specimen on the wet surface for various beam sizes ($2a$): I. constant loading, II. elliptical distribution. Solid line - theoretical plots at 1 MHz frequency; dash line - experimental measurements.

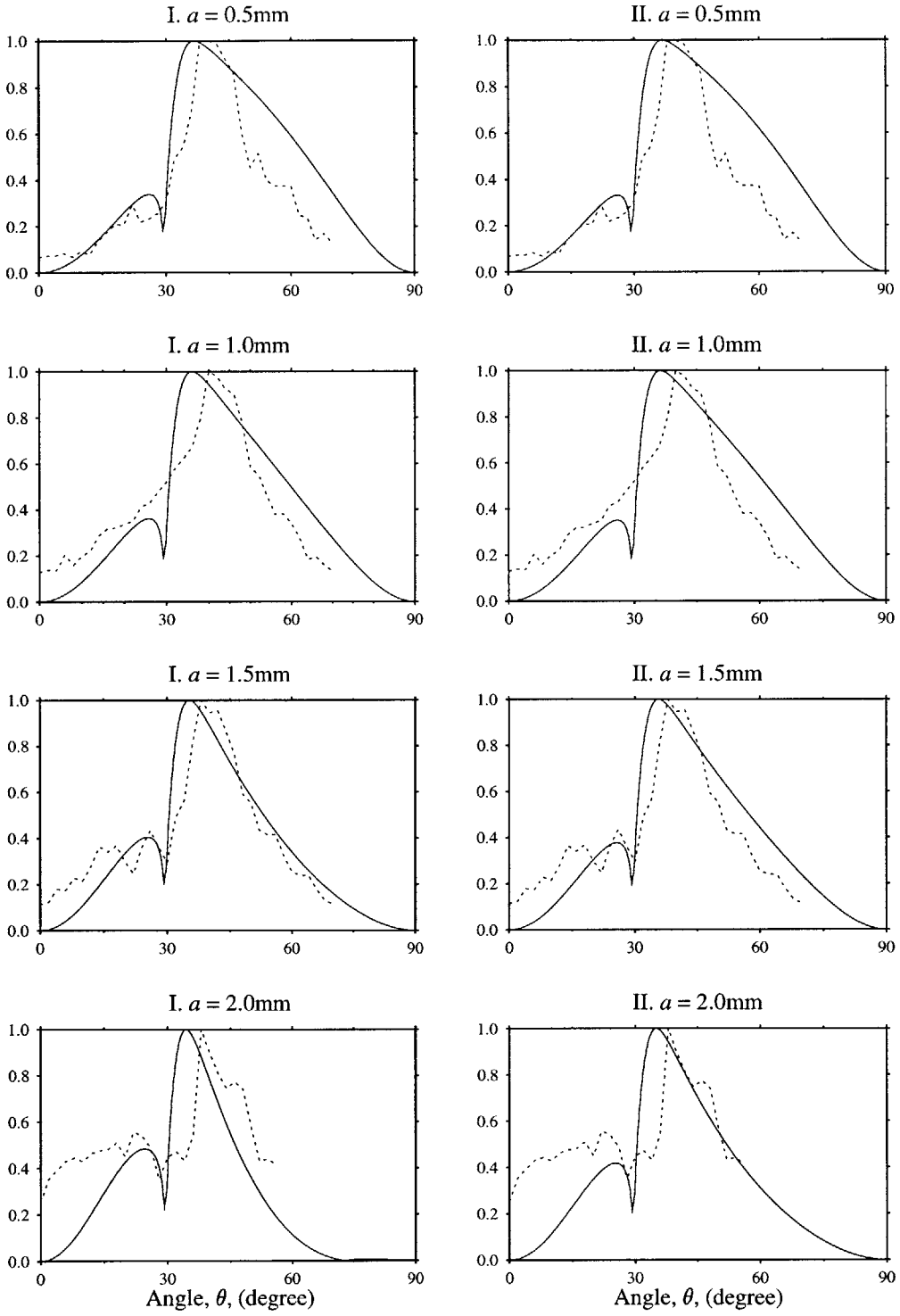

Figure 4-2: The measured out-of-plane displacements (U_y^T) as a function of propagating angle θ for the aluminum specimen on the wet surface for various beam sizes ($2a$): I. constant loading, II. elliptical distribution. Solid line - theoretical plots at 1 MHz frequency; dash line - experimental measurements.

These plots of the experimental and theoretical results show relatively small difference for the two models which is predicted in the theoretical discussion. For shear waves, the maximum U_y^T is measured experimentally at $\theta \approx 40°$ for various a, which is consistent with the theoretical plots of either constant loading or elliptical distribution models. The overall trend of each experimental plot is also observed to be in good agreement with the both theoretical results. This set of experiments are performed when a is increased up to 2 mm. Due to the limitation of the pulsed laser system, we can not further increase the beam size (which will significantly decrease the power density of the laser beam so that the signal-to-noise ratio is very low).

Figures. 4-3 and 4-4 respectively show the directivity patterns for longitudinal and shear waves, with PVDF transducer as the ultrasonic reception sensor. When constructing the theoretical directivity plots for both models, 5 MHz, which the center frequency of the transducer, is selected as the frequency of interest. Couplant is applied to stick the PVDF onto the sample surface. Similar trend of the change of the displacement amplitudes is shown, for example, the monotonously decreasing of the amplitudes and the highest values shows at $\theta = 0°$. But it is interesting to note that the experimental results is in a better agreement with those of elliptical distribution model. Same results are observed for shear waves. When $2a = 1$mm, the maximum of U_y^T appears at $\theta \approx 40°$, which verifies the theoretical prediction from both models, but it seems that elliptical distribution model is a better prediction in this case. The maximal U_y^T shifts to $\theta \approx 16°$ for the elliptical model when $2a = 2$mm, and keeps at $\theta \approx 40°$ for the constant model. Experimental results show a big peak at small angle $\theta = 16°$, which obviously matches the results of the elliptical model. Since the PVDF transducer is less sensitive than the cw laser, the experimental results couldn't been obtained for larger a such as $a = 2$mm due to the relatively low power density of the pulsed laser.

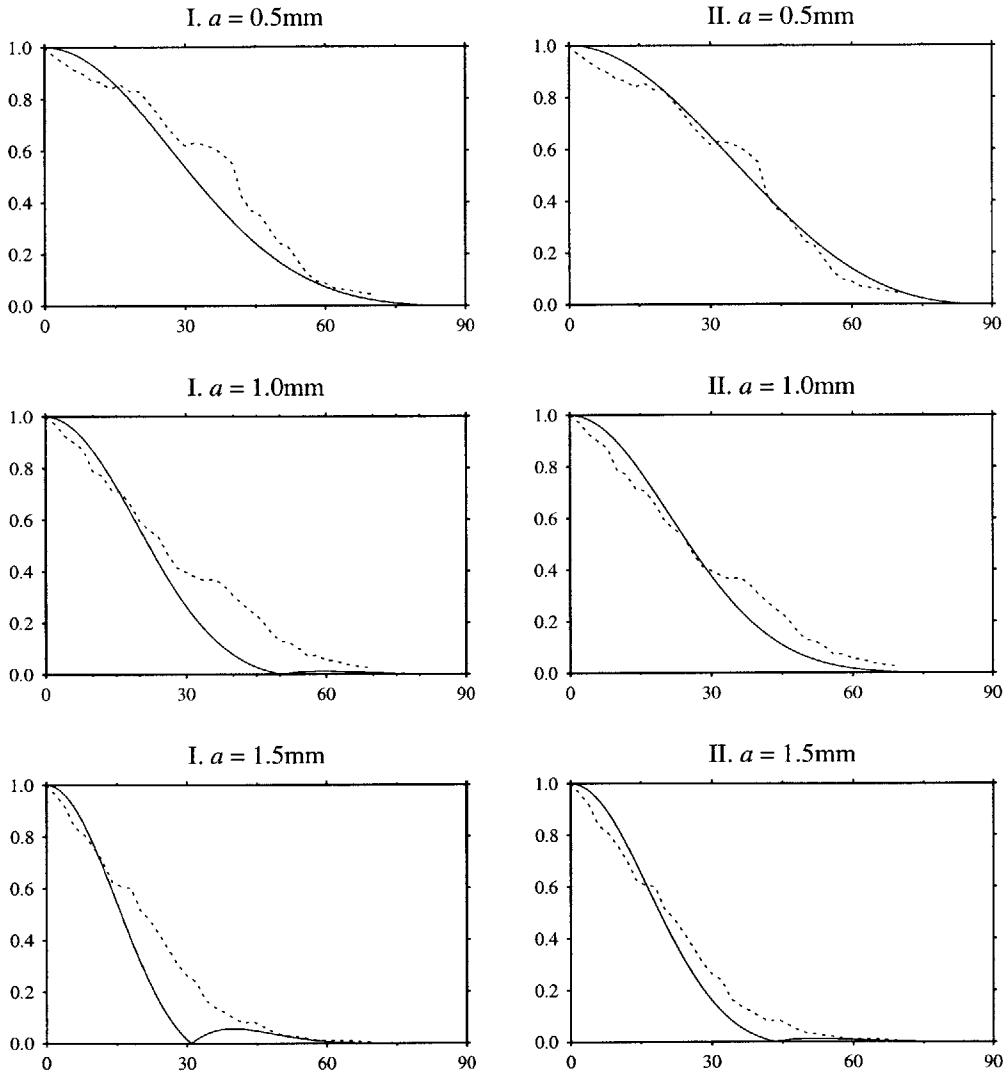

Figure 4-3: The measured out-of-plane displacements (U_y^L) as a function of propagating angle θ for the aluminum specimen on the wet surface for various beam sizes ($2a$): I. constant loading, II. elliptical distribution. Solid line - theoretical plots at 5 MHz frequency; dashed line - experimental measurements.

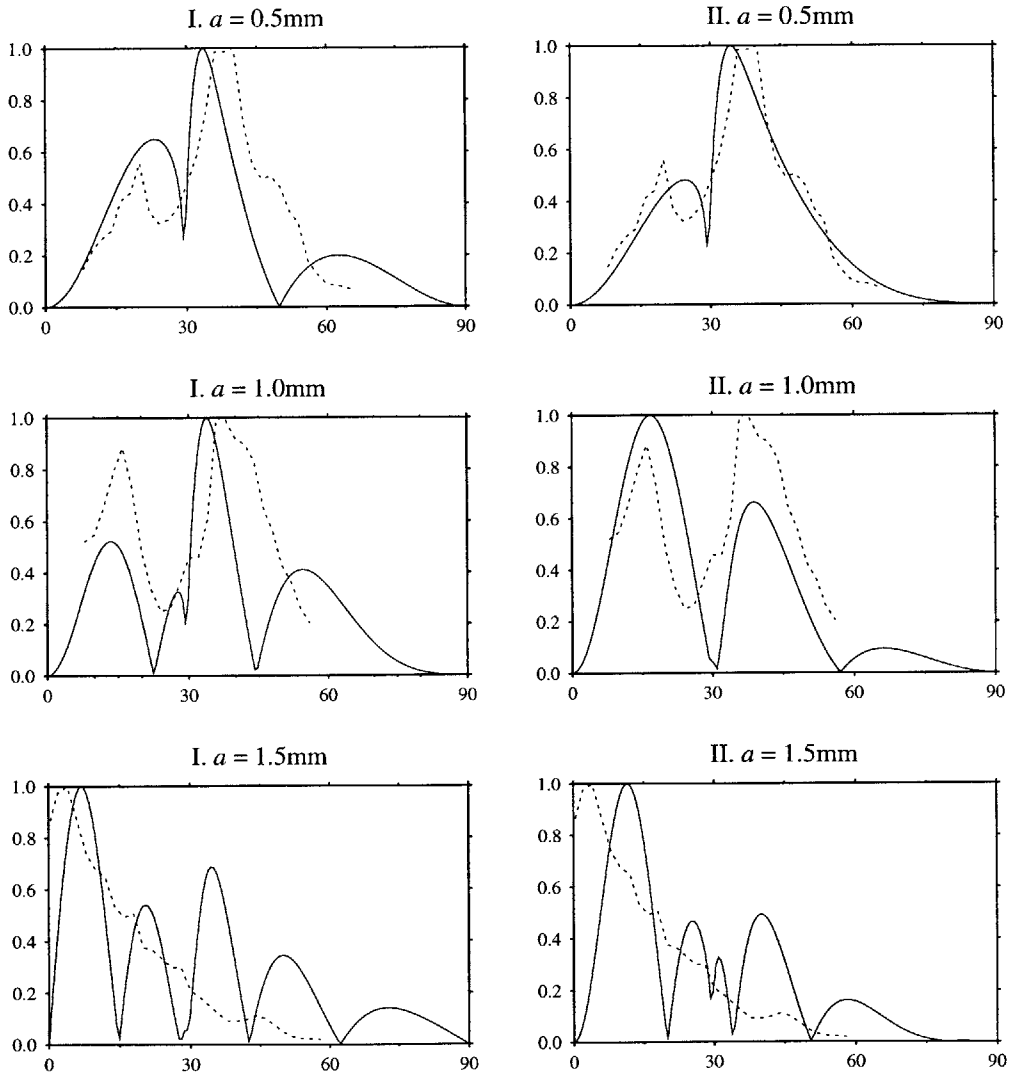

Figure 4-4: The measured out-of-plane displacements (U_y^T) as a function of propagating angle θ for the aluminum specimen on the wet surface for various beam sizes ($2a$): I. constant loading, II. elliptical distribution. Solid line - theoretical plots at 5 MHz frequency; dashed line - experimental measurements.

4.2 The influence of the beam size a

The directivity analysis shows that the directivity patterns of a certain radiation source is influenced by the source size a. It has been shown in Figs. 2-5 and 2-6 that the difference of the directivities between the constant loading and elliptical distribution cases is very small for small a at 1 MHz, and gets larger when a increases. This is verified in the experiments using cw laser system, when a is small such as 0.5, 1 and 1.5 mm, the experimental results match either of the two theoretical results well; but when $a = 2$ mm, the larger difference easily distinguishes the two models, and the experimental result is obviously closer to that of elliptical distribution case.

This phenomenon is also observed when the PVDF transducer is used. The directivity patterns change significantly as a increases. This is indicated by the shift of the maximal U_y^T. Compared the two models, it is noted that the directivity patterns can be better predicted by the elliptical distribution model when a increases.

4.3 The influence of the frequency f

Besides the influence of a, the frequency f of ultrasound also play an important role in the determination of the directivity patterns. Comparing Fig. 2-5 with Fig. 2-7, or Fig. 2-6 with Fig. 2-8, for a fixed a, larger differences between the constant loading model and elliptical distribution model are observed at 5 MHz, which can easily identify the two models. To see the difference experimentally, we can compare the two sets of experiments performed using the cw laser and PVDF transducer, respectively. By fixing a, the experimental plots at 5 MHz show an identifiable and better agreement with those of the elliptical model. See Figs. 4-3 and 4-4.

4.4 The influence of b

In the theoretical derivation of the elliptical distribution model, the ratio b/a describes the characteristics of the stress loading condition on the surface. For a fixed a, a large value of b implies higher reaction forces, resulting in high signal intensity, and vice versa. However, it is important to note that the value b does not make any influence on the directivity patterns. It is because of the following reasons. Consider two different values of b, say b_1 and b_2, as shown in Fig. 4-5. In these cases, the load magnitudes at two random positions R_1 and R_2 for b_1 and b_2 are respectively given as

$$\sigma_{zz}(R_1, b_1) = b_1\left(1 - \frac{R_1^2}{a^2}\right), \qquad \sigma_{zz}(R_2, b_1) = b_1\left(1 - \frac{R_2^2}{a^2}\right), \tag{4.1}$$

$$\sigma_{zz}(R_1, b_2) = b_2\left(1 - \frac{R_1^2}{a^2}\right), \qquad \sigma_{zz}(R_2, b_2) = b_2\left(1 - \frac{R_2^2}{a^2}\right). \tag{4.2}$$

Noting that the construction of directivity is based on Huygen's principle, the directivity is dependent on the distribution (shape) of loading, which can be described by considering

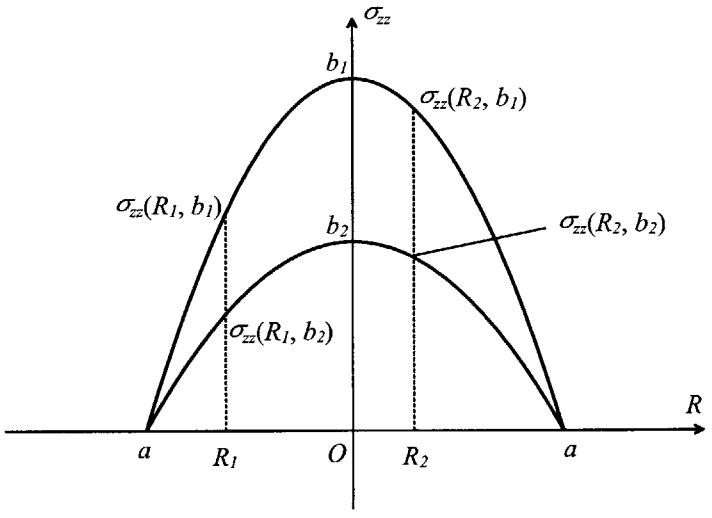

Figure 4-5: The influence of b

the values at two arbitrary points. In our case, the magnitude between the two points R_1 and R_2 can be written as

$$\frac{\sigma_{zz}(R_1, b_1)}{\sigma_{zz}(R_1, b_2)} = \frac{\sigma_{zz}(R_2, b_1)}{\sigma_{zz}(R_2, b_2)} = \frac{b_1}{b_2} . \tag{4.3}$$

Since this ratio is a constant, the parameter b does not make any contribution to the directivity. Mathematically, this phenomenon can be explained from Eq. (2.19) where the constant b is an independent variable of integration, i.e.,

$$\hat{\sigma}_{zz0} = b \int_0^a (1 - \frac{R^2}{a^2}) R J_0(\zeta R) dR .$$

Therefore, the directivity patterns are dependent only on the loading dimension a and wavenumbers k_L and k_T. It may be difficult to determine the absolute value of b experimentally, but this analysis makes it unnecessary to do that. This is our advantage, but it should be noted that this simplicity is resulted from the fact that we considered an ideally elliptical distribution. For different distributions, the directivity may be dependent on b.

Chapter 5

Summary and Conclusion

A new mathematical model, namely elliptical distribution model, is proposed in this thesis to predict the situation where the sample surface is modified by water or other liquids. The conventional constant loading model, which is derived from unmodified surface condition and is believed by other researchers to be applicable to the modified surface condition, is also presented as a comparison. The theoretical results, as well as experimental outcomes, indicate that although the two models are roughly close qualitatively in some circumstances, significant differences can exist when accurate results are desired.

Mathematically, the elliptical distribution model is more sophisticated than the constant loading model. The former involves more computational steps than the latter. Specifically, during the derivation of the elliptical model, higher order terms have to be kept in the expansion of Bessel functions. However, the complication of the elliptical distribution model does not compose a problem for its application. In fact, once the symbolic formula is obtained, for either model it takes very little time to calculate a specific directivity pattern given the corresponding parameters.

On the other hand, the experimental results show that the elliptical distribution model provides more accurate prediction for the directivity of modified surfaces than the constant loading model. The performance of the two models depends on the radius of the laser beam

and ultrasound frequency range. Particularly, the advantages of the elliptical distribution model are more prominent in the following situations. First, the size of the radiation source $2a$ is large. When the radius is small, the difference between the two models is negligible. However, the difference becomes more obvious when the radius increases. Second, the frequency of laser-generated ultrasound is high. The discrepancy between the two models is evident when the ultrasound frequency reaches 5 MHz. In both cases, the elliptical model agrees better with the experiment results.

One more interesting observation is that according to the mathematical derivation of the elliptical model, the power density of the pulsed laser beam doesn't make any contribution to the directivity. This conclusion is very important for the experimental measurement of the directivity. Experimentally, the directivity is measured in a point-by-point manner. It takes quite long time, with the average of three hours, to obtain a completed directivity plot. In practice, it is very difficult to keep a constant power density level for such a long time period due to the outside disturbances. But since the directivity is independent of the power density level, one can be assured that the directivity pattern obtained is a valid one. The variation of the power density level is not a factor for the measurement.

In conclusion, the elliptical loading model provides a better tool for the analysis of the directivity of laser generated ultrasound with modified surfaces.

Bibliography

[1] P. Mclntire, A.S. Birks, R.E. Green, Jr., *Nondestructive Testing Handbook*, 2nd edtion, v**7**, American Society for Nondestructive Testing, 1986

[2] ASM Handbook, *Nondestructive Evaluation and Quality Control*, Vol. **17**, ASM International, 1990

[3] J. Szilard, *Ultrasonic Testing*, John Wiley & Sons, New York, 1982

[4] C.B.Scruby and L.E.Drain, *Laser Ultrasonics: Techniques and Applications*, Adam Hilger, Bristol, UK, 1990

[5] J. Blitz, G. Simpson, *Ultrasonic Methods of Non-destructive Testing*, Chapman & Hall, New York, 1996

[6] G. F. Miller and H. Pursey, "The field and radiation impedence of mechanical radiators on the free surface of a semi-infinite isotropic solid", *Proceeding Royal Society* (London), A**223**, 1954, 521-541

[7] C.B. Scruby, "Quantitative studies of thermally generated elastic waves in laser-irradiated metals", *Journal of Applied Physics*, **51**(12), 1980, 6210–6216

[8] A.M. Aindow, R.J. Dewhurst, D.A. Hutchins, S.B. Palmer, "Laser-generated ultrasonic pulses at free metal surfaces", *Journal of the Acoustical Society of America*, v**69**, n**2**, Feburary 1981, 449–455

[9] D. A. Hutchins, R. J. Dewhurst, S. B. Palmer, "Directivity patterns of laser-generated ultrasound in aluminum", *The Journal of the Acoustic Society of America*, **70**(5), Nov 1981. 1362–1369

[10] D.A. Hutchins, R. J. Dewhurst, S. B. Palmer, "Laser generated ultrasound at modified metal surfaces", *Ultrasonics*, v**19**(3), 1981, 103–108

[11] R.J. Dewhurst, D.A. Hutchins, S.B. Palmer, "Quantitative measurements of laser-generated acoustic waveforms", *Journal of Applied Physics*, **53**(6), June 1982, 4064–4071

[12] L.R.F.Rose, "Point-source representation for laser-generated ultrasound", *The Journal of the Acoustic Society of America*, **75**(3), March 1984, 723–732

[13] D.A. Hutchins, "Mechanism of pulsed photoacoustic generation", *Canadian Journal of Physics*, **64**, 1986, 1247–1264

[14] C.B. Scruby, "Some applications of laser ultrasound", *Ultrasonics*, v**27**, July 1989, 195–209

[15] S.J. Davies, *et al.*, "Laser-generated ultrasound: its properties, mechanisms and multifarious applications", *Journal of Physics-D*, **26**, 1993, 329–348

[16] P. Zhang, C.F. Ying, J. Shen, "Directivity patterns of laser thermoelastically generated ultrasound in metal with consideration of thermal conductivity", *Ultrasonics*, v**35**, 1997, 233–240

[17] Y. Wu, D. Shi, Y. He, "Study of the directivity of laser generated ultrasound in solids", *Journal of Applied Physics*, **83**(3), 1998, 1207–1212

[18] S.N. Hopko, I.C. Ume, "Laser generated ultrasound by material ablation using fiber optic delivery", *Ultrasonics*, **37**, 1999, 1–7

[19] D.H. Hurley, J.B. Spicer, "Point-source representation for laser-generated ultrasound in an elastic, transversely isotropic half-space", *Journal of Applied Physics*, **86**(6), 1999, 3423–3427

[20] J.R. Bernstein, J.B. Spicer, "Line source representation for laser-generated ultrasound in aluminum", *THe Journal of the Acoustic Society of America*, **107**(3), 2000, 1352–1357

[21] G.M. Graham, J. Yang, C. Ume, "Laser ultrasound directivity in CS-3 ceramic", *Material Evaluation*, 1994, 607–610

[22] Y. Bai, L. Pei, Q. Fang, "Experimental study of directivity patterns of laser ultrasound in an unpolarized PZT ceramic in the thermoelastic regime", *Ultrasonics*, v**32**(5), 1994, 323–326

[23] Y. Bai, L. Pei, Q. Fang, "Experimental studies of directivity patterns of laser ultrasound in neutral glasses", *Ultrasonics*, v**33**(6), 1995, 429–436

[24] J.A. Fox, "Effect of water and paint coatings on laser-irradiated targets", *Applied Physics Letters*, **24**(10), 1974, 461–464